European Journal of Mechanics / A Solids 71 (2018) 258–277

Contents lists available at ScienceDirect

European Journal of Mechanics / A Solids

journal homepage: www.elsevier.com/locate/ejmsol

Assessment of porosity influence on vibration and static behaviour of functionally graded magneto-electro-elastic plate: A finite element study

M.C. Kiran, S.C. Kattimani*

Department of Mechanical Engineering, National Institute of Technology Karnataka, Surathkal 575025, India

ARTICLE INFO

Keywords:
Porosity
Functionally graded
Magneto-electro-elastic
Free vibration
Finite element
Static behaviour

ABSTRACT

In this paper, the free vibration characteristics and the static behaviour of porous functionally graded magneto-electro-elastic (FGMEE) plate is investigated using finite element method. The porosities arise due to the maladies in the fabrication processes and such porosities or micro-voids are accounted using modified power law. Influence of different porosity distributions on the behaviour of PFGMEE plate are considered in this study. The through thickness variation of material properties is achieved to obtain a functionally graded MEE plate. The coupled constitutive equations along with the principle of virtual work are used to develop a FE model for FGMEE plates. Influence of various porosity distributions on the structural behaviour of the plate is thoroughly investigated. The effect of porosity volume and material gradient index on the free vibration and static behaviour is explicitly studied. This study also includes the evaluation of the effect of geometrical parameters such as thickness ratio, aspect ratio, and boundary condition on the structural characteristics of porous FGMEE plate.

1. Introduction

Magneto-electro-elastic (MEE) materials are the combination of piezoelectric, Barium Titanate ($BaTiO_3$) and magnetostrictive, Cobalt Ferrite ($CoFe_2O_4$) materials. Such materials exhibit magneto-electric coupling which is absent in their individual phases (Boomgaard and Born, 1978). This unique property facilitates MEE materials to be largely sought in sensors and actuators applications. MEE composites exist in layered, multiphase, and functionally graded forms (Buchanan, 2004). Multilayered MEE plates are extensively investigated to assess their free vibration characteristics, buckling, and static behaviour under various loading conditions (Kiran and Kattimani, 2017, 2018a; Ramirez et al., 2006; Chen et al., 2014; Lage et al., 2004; Simoes Moita et al., 2009). Pan and his co-researchers (Pan, 2001; Pan and Heyliger, 2003; Pan and Han, 2005) proposed various analytical solutions to evaluate free vibration and static response of MEE plate. The behavioural study of MEE plate for free vibration and large deflection was established by Millazo (Milazzo, 2014a, 2014b, 2016; Kattimani and Ray, 2014a) via various methodologies. Kattimani and Ray, 2014a, 2014b discussed active constrained layered damping as an effective measure to control non-linear vibrations in MEE plates and shells. The scaled boundary FE method was implemented by Liu et al. (2016) to ascertain the higher order solutions for MEE plate composed of non-uniform material. Wakmanski and Pan (Waksmanski and Pan, 2016) evaluated free vibration of multilayered MEE plate with non local effect using 3-D analytical solutions. To reduce or eliminate the interface stresses existing in laminated composites, functionally graded materials were developed. The FG material properties vary throughout the thickness. The presence of functionally graded material in various applications has been increasing with the innovation in cutting edge manufacturing techniques (Mortensen and Suresh, 1995; Pompe et al., 2003; Miyamoto et al., 2013). The various structural characteristics of FGMEE material have been explicitly studied by many researchers (Ebrahimi et al., 2009; Ebrahimi and Rastgoo, 2009, 2011; Vinyas and Kattimani, 2017). Kattimani and Ray (2015) researched large-amplitude vibration responses of FG MEE plates. Recently, Kiran and Kattimani (2018b) investigated the frequency and static characteristics of skew-FGMEE plate.

The recent development in FGM includes the graded porosity structures. The pores in the microstructures of such structural materials are accounted via local density of the material. The methods to prepare FGMs are a trending area of research capturing attention of many researchers. The preparation method includes powder metallurgy, vapour deposition, self propagation, centrifugal casting, and magnetic separation (Khor and Gu, 2000; Barati, 2018; Watanabe et al., 2001; Song et al., 2007; Peng et al., 2007). Although many preparation methods are available, the sintering process is preferred due to its cost effectiveness. The FGMs prepared using sintering process possesses micro-voids or porosities due to the different solidification rate of material constituents (Zhu et al., 2001). A study by Wattanasakulpong et al. (2012) projects

* Corresponding author.
E-mail address: sck@nitk.ac.in (S.C. Kattimani).

https://doi.org/10.1016/j.euromechsol.2018.04.006
Received 17 January 2018; Received in revised form 4 April 2018; Accepted 9 April 2018
Available online 11 April 2018

the importance of considering porosity factor in the design and analysis of FGMs. Wang et al. (2017) investigated the vibration characteristics of FG plates with porosities. Recently, Kiran and Kattimani (2018c) investigated the influence of porosities on the skew FGMEE plate. Ebrahimi et al. (2017a) analysed the vibration characteristics of MEE heterogeneous porous material plates resting on elastic foundations. Aero-hygro-thermal stability analysis of higher-order refined supersonic FGM panels with even and uneven porosity distributions was studied by Barati and Shahverdi (2017). Using refined four-variable theory, Barati et al. (2017) studied the electro-mechanical vibration of smart piezoelectric FG plates with porosities. Ebrahimi et al. (2017b) studied the free vibration of smart porous plates subjected to various physical fields considering neutral surface position.

Though, the recent developments in manufacturing techniques have improved significantly, the porosity is a common defect often observed in FGMs. Hence, it is intended to develop a suitable FE model to study the behaviour of FGMEE plates accounting the inherent porosity in the material. Studies on static analysis and free vibration characteristics of $BaTiO_3$—$CoFe_2O_4$ plates with porosity distribution are scarce in the literature. Hence, in this article, the finite element formulation to evaluate the free vibration and static characteristics of porous FGMEE plate for different porosity models is considered for evaluation. The effect of different porosity distribution, porosity volume index, and gradient index affecting the structural behaviour of porous FGMEE plate is extensively investigated. Further, the effect of thickness ratio, aspect ratio, and boundary condition is studied.

2. Problem description and governing equation

A schematic diagram of a porous functionally graded magneto-electro-elastic (FGMEE) plate with a Cartesian coordinate system attached to the corner of the plate is shown in Fig. 1. The length, the width and the total thickness of the plate are *a*, *b* and *h*, respectively. The material properties of the porous FGMEE plate are assumed to vary across the thickness. The bottom surface of the plate is piezoelectric ($BaTiO_3$) and the top surface being magnetostrictive ($CoFe_2O_4$). The plate model involved in the present analysis is developed by Hilderbrand et al. (Hildebrand et al., 1949). The displacement components *u*, *v* and *w* along *x*-, *y*-, and *z*-direction at any point in the porous FGMEE plate can be represented by (Hildebrand et al., 1949)

$$\begin{aligned} u(x,y,z,t) &= u_0(x,y,t) + z\theta_x(x,y,t) \\ v(x,y,z,t) &= v_0(x,y,t) + z\theta_y(x,y,t) \\ w(x,y,z,t) &= w_0(x,y,t) + z\theta_z(x,y,t) + z^2\kappa_z(x,y,t) \end{aligned} \tag{1}$$

where, u_0 and v_0 are the translational displacements at any point on the mid-plane of the plate along *x*- and *y*-directions while w_0 is the transverse displacement along *z*-direction at any point in the porous FGMEE plate. θ_x denote the generalized rotation of the normal to the middle plane of the porous FGMEE plate about the *y*-axis while θ_y denote the generalized rotation of the normal to the middle plane of the porous FGMEE plate about the *x* - axis. θ_z and κ_z are the generalized rotational displacements for the porous FGMEE plate with respect to the thickness coordinate. For the ease of computation, rotational and translational displacements are considered separately as follows:

$$\{d_t\} = [u_0\ v_0\ w_0]^{\mathrm{T}} \{d_r\} = [\theta_x\ \theta_y\ \theta_z\ \kappa_z]^T \tag{2}$$

The shear locking in the thin structures is overcome by employing the selective integration rule and also facilitates the computation of elemental stiffness matrices linked with the transverse shear deformation in detail. This specific need is achieved by considering the state of strain at any point in the plate, separated by in-plane and transverse normal strain vector $\{\varepsilon_b\}$ and the transverse shear strain vector $\{\varepsilon_s\}$ given as

$$\{\varepsilon_b\} = [\varepsilon_x\ \varepsilon_y\ \varepsilon_z\ \nu_{xy}]^T \{\varepsilon_s\} = [\nu_{xz}\ \nu_{yz}]^T \tag{3}$$

where, ε_x, ε_y and ε_z represent the normal strains along *x*-, *y*- and *z*-directions, respectively; ν_{xy} represents the in-plane shear strain, ν_{xz} and ν_{yz} are the transverse or out of plane shear strains. Making use of the displacement field given in Eq. (1) and from the linear strain-displacement relations, the strain vectors $\{\varepsilon_b\}$ and $\{\varepsilon_s\}$ defining the state of inplane, transverse normal and transverse shear strain at any point in the porous FGMEE plate can be expressed as

$$\{\varepsilon_b\} = \{\varepsilon_{bt}\} + [Z_1]\{\varepsilon_{rb}\}\{\varepsilon_s\} = \{\varepsilon_{ts}\} + [Z_2]\{\varepsilon_{rs}\} \tag{4}$$

wherein the transformation matrices $[Z_1]$ and $[Z_2]$ are expressed as

$$[Z_1] = \begin{bmatrix} z & 0 & 0 & 0 & 0 \\ 0 & z & 0 & 0 & 0 \\ 0 & 0 & 0 & 1 & 2z \\ 0 & 0 & z & 0 & 0 \end{bmatrix} [Z_2] = \begin{bmatrix} 1 & 0 & z & 0 & z^2 & 0 \\ 0 & 1 & 0 & z & 0 & z^2 \end{bmatrix}$$

The generalized strain vectors appearing in Eq. (4) are given by

$$\{\varepsilon_{bt}\} = \begin{bmatrix} \frac{\partial u_0}{\partial x} & \frac{\partial v_0}{\partial y} & 0 & \frac{\partial u_0}{\partial y} + \frac{\partial v_0}{\partial x} \end{bmatrix} \{\varepsilon_{ts}\} = \begin{bmatrix} \frac{\partial w_0}{\partial x} & \frac{\partial w_0}{\partial y} \end{bmatrix}$$

$$\{\varepsilon_{rb}\} = \begin{bmatrix} \frac{\partial \theta_x}{\partial x} & \frac{\partial \theta_y}{\partial y} & \frac{\partial \theta_x}{\partial x} + \frac{\partial v_0}{\partial x} & \theta_z & \kappa_z \end{bmatrix} \text{and} \{\varepsilon_{rs}\}$$

$$= \begin{bmatrix} \theta_x & \theta_y & \frac{\partial \theta_z}{\partial x} & \frac{\partial \theta_z}{\partial y} & \frac{\partial \kappa_z}{\partial x} & \frac{\partial \kappa_z}{\partial y} \end{bmatrix}^T$$

Analogous to the strain vectors given in Eq. (3), the state of stress at any point in the porous FGMEE plate can be written as follows:

$$\{\boldsymbol{\sigma}_b\} = [\sigma_x\ \sigma_y\ \sigma_{xy}\ \sigma_z]^{\mathrm{T}} \{\boldsymbol{\sigma}_s\} = [\tau_{xz}\ \tau_{yz}]^{\mathrm{T}} \tag{5}$$

in which, σ_x, σ_y and σ_z are the normal stresses along *x*-, *y*- and *z*-directions, respectively; σ_{xy} is the in-plane shear stress; τ_{xz} and τ_{yz} are the transverse shear stresses along *xz*- and *yz*-directions, respectively. Considering the effect of coupled fields, the constitutive equations for the porous FGMEE plate can be expressed as follows:

$$\{\sigma_b\} = [\overline{C}_b(z)]\{\varepsilon_b\} - \{e_b(z)\}E_z - \{q_b(z)\}H_z\{\boldsymbol{\sigma}_s\} = [\overline{C}_s(z)]\{\varepsilon_s\} \tag{6a}$$

$$D_z = \{e_b(z)\}^{\mathrm{T}}\{\varepsilon_b\} + \xi_{33}(z)E_z + d_{33}(z)H_z \tag{6b}$$

$$B_z = \{q_b(z)\}^{\mathrm{T}}\{\varepsilon_b\} + d_{33}(z)E_z + \mu_{33}(z)H_z \tag{6c}$$

where, $[\overline{C}_b(z)]$ and $[\overline{C}_s(z)]$ are the functionally graded material coefficient matrices given as $[\overline{C}_b(z)] = \begin{bmatrix} \overline{C}_{11}(z) & \overline{C}_{12}(z) & \overline{C}_{13}(z) & \overline{C}_{16}(z) \\ \overline{C}_{12}(z) & \overline{C}_{22}(z) & \overline{C}_{23}(z) & \overline{C}_{26}(z) \\ \overline{C}_{13}(z) & \overline{C}_{23}(z) & \overline{C}_{33}(z) & \overline{C}_{36}(z) \\ \overline{C}_{16}(z) & \overline{C}_{26}(z) & \overline{C}_{36}(z) & \overline{C}_{66}(z) \end{bmatrix}$

$[\overline{C}_s(z)] = \begin{bmatrix} \overline{C}_{55}(z) & \overline{C}_{45}(z) \\ \overline{C}_{45}(z) & \overline{C}_{44}(z) \end{bmatrix}$ (7).While, $\xi_{33}(z)$ and $\mu_{33}(z)$ are the dielectric

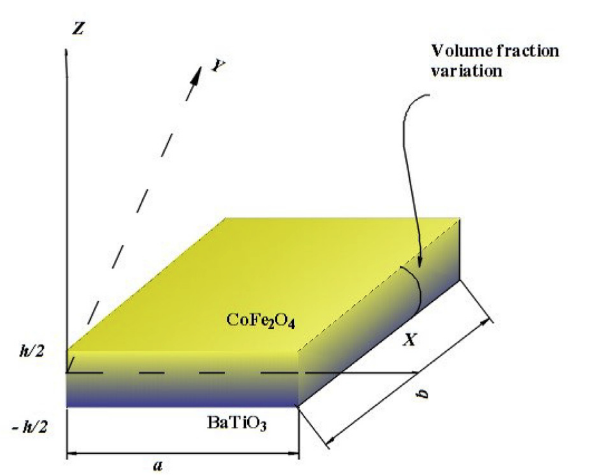

Fig. 1. Functionally graded MEE plate.

constant and the magnetic permeability constant, respectively; $d_{33}(z)$ is the electromagnetic coefficient. The electric displacement, the electric field, the magnetic induction and the magnetic field along the z-direction are represented by D_z, E_z, B_z and H_z, respectively. The electric coefficient matrix $\{e_b(z)\}$ and the magnetic coefficient matrix $\{q_b(z)\}$ are given by

$$\{e_b(z)\} = \begin{Bmatrix} e_{31}(z) \\ e_{32}(z) \\ e_{33}(z) \\ e_{36}(z) \end{Bmatrix} \{q_b(z)\} = \begin{Bmatrix} q_{31}(z) \\ q_{32}(z) \\ q_{33}(z) \\ q_{36}(z) \end{Bmatrix} \tag{8}$$

The material coefficients accounting different porosity distribution is given by modified power law distribution as follows:

$$\begin{aligned}
\overline{C}_{fg}(z) &= C_F + (C_B - C_F) \times V - (C_B + C_F) \times (m/2) \times V_p \\
\overline{\rho}_{fg}(z) &= \rho_F + (\rho_B - \rho_F) \times V - (\rho_B + \rho_F) \times (m/2) \times V_p \\
\overline{e}_{fg}(z) &= e_F + (e_B - e_F) \times V - (e_B + e_F) \times (m/2) \times V_p \\
\overline{q}_{fg}(z) &= q_F + (q_B - q_F) \times V - (q_B + q_F) \times (m/2) \times V_p \\
\overline{\xi}_{fg}(z) &= \xi_F + (\xi_B - \xi_F) \times V - (\xi_B + \xi_F) \times (m/2) \times V_p \\
\mu_{fg}(z) &= \mu_F + (\mu_B - \mu_F) \times V - (\mu_B + \mu_F) \times (m/2) \times V_p
\end{aligned} \tag{9}$$

where, the subscripts B and F refers to $BaTiO_3$ and $CoFe_2O_4$, respectively, m is the porosity index ($0 < m < 1$) and V_p is the generalized term to represent the different porosity distribution such as Vu, Vo, Vx, and Vv as shown in Fig. 2 and are given as follows:

(a) Uniform porosity distribution, Vu

$$V_u = 1 \tag{10a}$$

(b) O-shaped centralized porosity distribution, Vo

$$V_o = \left\{1 - \frac{2|z|}{h}\right\} \tag{10b}$$

(c) High density of porosity at the top and bottom while low at the mid span i.e., Vx

$$V_x = \left\{\frac{2|z|}{h}\right\} \tag{10c}$$

(d) Higher porosity density at the top and lower at the bottom, Vv

$$V_v = \left\{1 + \frac{2|z|}{h}\right\} \tag{10d}$$

while, V is given by

$$V = \left\{\left(\frac{z}{h}\right) + \left(\frac{1}{2}\right)\right\}^{\eta} \tag{11}$$

wherein, η is the power law gradient.

Employing the principle of virtual work (Kattimani and Ray, 2015), the governing equations for the porous FGMEE plate is established as

$$\left(\int_{\Lambda} \delta\{\varepsilon_b\}\{\boldsymbol{\sigma}_b\} d\Lambda + \int_{\Lambda} \delta\{\varepsilon_s\}\{\boldsymbol{\sigma}_s\} d\Lambda + \int_{\Lambda} \delta\{d_t\}^T \rho(z)\{\ddot{d}_t\} d\Lambda\right) \int_{\Lambda} \delta E_z D_z d\Lambda - \int_{\Lambda} \delta H_z B_z d\Lambda - \int_{A} \delta\{d_t\}^T F_t dA^{el} = 0 \tag{12}$$

where, Λ indicates the volume of the plate, F_t is the applied force with sinusoidal distribution on the top surface area A^{el}, $\rho(z)$ denotes the mass density variation through the thickness. E_z and D_z are the electric fields and the electric displacements, respectively, while H_z and B_z are the magnetic fields and magnetic induction, respectively. The transverse electric field (E_z) related to the electric potential and the transverse magnetic field (H_z) is related to the magnetic potential in accordance with Maxwell's equation as follows (Kattimani and Ray, 2015):

$$E_z = -\frac{\partial \phi}{\partial z} \text{and} H_z = -\frac{\partial \psi}{\partial z} \tag{13}$$

where, ϕ and ψ are the electric and magnetic potential. It is noteworthy to mention that the thickness of porous FGMEE plate is very small and hence, the variation of electric potential and magnetic potential functions can be assumed to be linear across the plate thickness.

3. Finite element formulation

The porous FGMEE plate is discretized using eight noded iso-parametric elements. In accordance with Eq. (3), the generalized displacement vectors $\{d_{ti}\}$ and $\{d_{ri}\}$ associated with the ith node (where, $i = 1, 2, 3, \ldots, 8$) of an element can be expressed as

$$\{d_{ti}\} = [u_{0i}\ v_{0i}\ w_{0i}]^T \text{and} \{d_{ri}\} = [\theta_{xi}\ \theta_{yi}\ \theta_{zi}\ \kappa_{zi}]^T \tag{14}$$

At any point within the element, the generalized displacement vectors $\{d_t\}$ and $\{d_r\}$, the magnetic potential vector $\{\psi\}$ and the electric potential vector $\{\phi\}$ can be expressed in terms of nodal generalized displacement vectors $\{d_t^{el}\}$ and $\{d_r^{el}\}$, the nodal magnetic potential vector $\{\psi^{el}\}$ and the nodal electric potential vector $\{\phi^{el}\}$, respectively, as follows:

$$\begin{aligned}
&[d_t] = [N_t]\{d_t^{el}\}\{d_r\} = [N_r]\{d_r^{el}\} \\
&\{\phi\} = [N_\phi]\{\phi^{el}\}\{\psi\} = [N_\psi]\{\psi^{el}\}
\end{aligned} \tag{15}$$

in which,

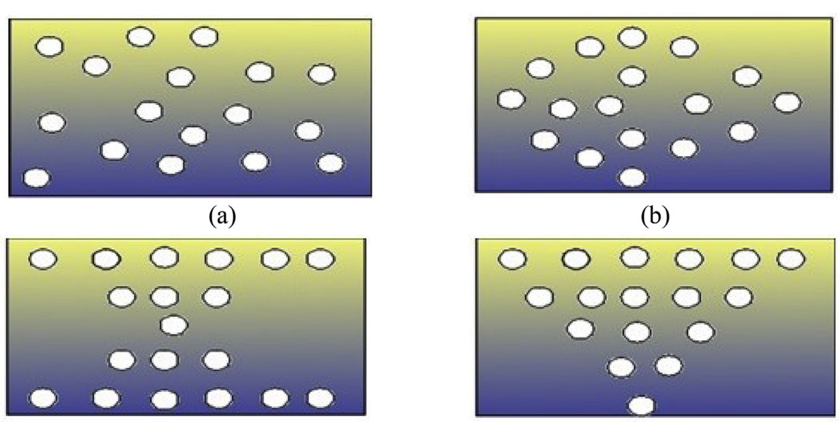

Fig. 2. Porosity distribution (a) Vu (b) Vo (c) Vx (d) Vv.

$$\{d_t^{el}\} = [\{d_{t1}^{el}\}^T\{d_{t2}^{el}\}^T \ . \ . \ . \ \{d_{t8}^{el}\}^T]^T\{d_r^{el}\} = [\{d_{r1}^{el}\}^T\{d_{r2}^{el}\}^T \ . \ . \ . \ \{d_{r8}^{el}\}^T]^T$$
$$\{\phi^{el}\} = \{\phi_1 \ \phi_2 \ . \ . \ . \phi_8\}^T\{\psi^{el}\} = \{\psi_1 \ \psi_2 \ . \ . \ . \ \psi_8\}^T$$
$$[N_t] = [N_{t1} N_{t2} \ . \ . \ . \ N_{t8}]^T[N_r] = [N_{r1} N_{r2} \ . \ . \ . \ N_{r8}]^T$$
$$[N_\phi] = [N_{\phi1} N_{\phi2} \ . \ . \ . \ N_{\phi8}]^T[N_\psi] = [N_{\psi1} N_{\psi2} \ . \ . \ . \ N_{\psi8}]^T$$
$$N_{ti} = n_i I_t, \quad N_{ri} = n_i I_r \tag{16}$$

where $[N_t]$, $[N_r]$, $[N_\phi]$ and $[N_\psi]$ are the shape function matrices, respectively; I_t and I_r are the identity matrices, respectively. n_i is the shape function of natural coordinate associated with the ith node. ϕ_i (where, i = 1, 2, 3,…, 8) are the electric potential degrees of freedom and ψ_i are the magnetic potential degrees of freedom. Using Eqs. 13–16, the transverse electric field (E_z) and the transverse magnetic field (H_z) are given by

$$E_z = -\frac{1}{h}[N_\phi]\{\phi^{el}\} \text{and} H_z = -\frac{1}{h}[N_\psi]\{\psi^{el}\} \tag{17}$$

Now, using Eqs. (4) and (16), the generalized strain vectors at any point within the element can be expressed in terms of the nodal generalized strain vectors as follows:

$$\{\varepsilon_{bt}\} = [b_{tb}]\{d_t^{el}\}\{\varepsilon_{br}\} = [b_{rb}]\{d_r^{el}\}$$
$$\{\varepsilon_{ts}\} = [b_{ts}]\{d_t^{el}\}\{\varepsilon_{rs}\} = [b_{rs}]\{d_r^{el}\} \tag{18}$$

in which, $[b_{tb}]$, $[b_{rb}]$, $[b_{ts}]$ and $[b_{rs}]$ are the nodal strain-displacement matrices. Substituting Eqs. (4) and (6) and (16)–(18) into Eq. (12) and simplifying, we obtain the elemental equations of motion for the porous FGMEE plate as follows:

$$[M^{el}]\{\ddot{d}_t^{el}\} + [k_{tt}^{el}]\{d_t^{el}\} + [k_{tr}^{el}]\{d_r^{el}\} + [k_{t\phi}^{el}]\{\phi^{el}\} + [k_{t\psi}^{el}]\{\psi^{el}\} = \{F_t^{el}\} \tag{19}$$

$$[k_{tr}^{el}]^T\{d_t^{el}\} + [k_{rr}^{el}]\{d_r^{el}\} + [k_{r\phi}^{el}]\{\phi^{el}\} + [k_{r\psi}^{el}]\{\psi^{el}\} = 0 \tag{20}$$

$$[k_{t\phi}^{el}]^T\{d_t^{el}\} + [k_{r\phi}^{el}]^T\{d_r^{el}\} - [k_{\phi\phi}^{el}]\{\phi^{el}\} = 0 \tag{21}$$

$$[k_{t\psi}^{el}]^T\{d_t^{el}\} + [k_{r\psi}^{el}]^T\{d_r^{el}\} - [k_{\psi\psi}^{el}]\{\psi^{el}\} = 0 \tag{22}$$

The matrices and the vectors appearing in Eqs. 19–22 are the elemental mass matrix $[M^{el}]$, the elemental elastic stiffness matrices $[k_{tt}^{el}]$, $[k_{tr}^{el}]$ and $[k_{rr}^{el}]$, the elemental electro-elastic coupling stiffness matrices and the elemental magneto-elastic coupling stiffness matrices are $[k_{t\phi}^{el}]$, $[k_{r\phi}^{el}]$ and $[k_{t\psi}^{el}]$, $[k_{r\psi}^{el}]$, respectively; $\{F_t^{el}\}$ is the elemental mechanical load vector; $[k_{\phi\phi}^{el}]$ and $[k_{\psi\psi}^{el}]$ are the elemental electric and elemental magnetic stiffness matrices, respectively. The elemental matrices and vectors appearing in Eqs. 19–22 are provided in the Appendix.

The elemental equations of motion in are assembled to obtain the global equations of motion of the porous FGMEE plate as follows:

$$[M]\{\ddot{d}_t\} + [k_{tt}^g]\{d_t\} + [k_{tr}^g]\{d_r\} + [k_{t\phi}^g]\{\phi\} + [k_{t\psi}^g]\{\psi\} = \{F_t\} \tag{23}$$

$$[k_{tr}^g]^T\{d_t\} + [k_{rr}^g]\{d_r\} + \{k_{r\phi}^g\}\{\phi\} + [k_{r\psi}^g]\{\psi\} = 0 \tag{24}$$

$$[k_{t\phi}^g]^T\{d_t\} + [k_{r\phi}^g]^T\{d_r\} - [k_{\phi\phi}^g]\{\phi\} = 0 \tag{25}$$

$$[k_{t\psi}^g]^T\{d_t\} + [k_{r\psi}^g]^T\{d_r\} - [k_{\psi\psi}^g]\{\psi\} = 0 \tag{26}$$

where, [M] is the global mass matrix; $[k_{tt}^g]$, $[k_{tr}^g]$ and $[k_{rr}^g]$ are the global elastic stiffness matrices; $[k_{t\phi}^g]$ and $[k_{r\phi}^g]$ are the global electro-elastic coupling stiffness matrices; $[k_{t\psi}^g]$ and $[k_{r\psi}^g]$ are the global magneto-elastic coupling stiffness matrices; $\{F_t\}$ is the global mechanical load vector; $[k_{\phi\phi}^g]$ and $[k_{\psi\psi}^g]$ are the global electric and the global magnetic stiffness matrices, respectively. Solving the global equations of motion (Eq. (24)–(26) to obtain global generalized displacement vector $\{d_t\}$ and $\{d_r\}$ by condensing the global degrees of freedom for $\{\phi\}$ and $\{\psi\}$ in terms of $\{d_r\}$ as follows:

$$\{\psi\} = \{k_{\psi\psi}^g\}^{-1}[k_{t\psi}^g]^T d_t + [k_{\psi\psi}^g]^{-1}[k_{r\psi}^g]^T\{d_r\}$$
$$\{\phi\} = [k_{\phi\phi}^g]^{-1}[k_{t\phi}^g]^T\{d_t\} + [k_{\phi\phi}^g]^{-1}[k_{r\phi}^g]^T\{d_r\}$$
$$\{d_r\} = -[K_3]^{-1}[K_2]^T\{d_t\} \tag{27}$$

Now, substituting Eq. (27) in Eq. (23) and upon simplification, we obtain the global equations of motion in terms of the global translational degrees of freedom as follows:

$$[M]\{\ddot{d}_t\} + ([K_1] - [K_2][K_3]^{-1}[K_2]^T)\{d_t\} = \{F_t\}$$
$$[M]\{\ddot{d}_t\} + [K]\{d_t\} = \{F_t\} \text{and}$$
$$[K] = ([K_1] - [K_2][K_3]^{-1}[K_2]^T) \tag{28}$$

where, the global aggrandized matrices are given as follows:

$$[K_1] = [k_{tt}^g] + [k_{t\phi}^g][k_{\phi\phi}^g]^{-1}[k_{t\phi}^g]^T + [k_{t\psi}^g][k_{\psi\psi}^g]^{-1}[k_{t\psi}^g]^T$$

$$[K_2] = [k_{tr}^g] + [k_{t\phi}^g][k_{\phi\phi}^g]^{-1}[k_{r\phi}^g]^T + [k_{t\psi}^g][k_{\psi\psi}^g]^{-1}[k_{r\psi}^g]^T$$

$$[K_3] = [k_{rr}^g] + [k_{r\phi}^g][k_{\phi\phi}^g]^{-1}[k_{r\phi}^g]^T + [k_{r\psi}^g][k_{\psi\psi}^g]^{-1}[k_{r\psi}^g]^T$$

3.1. Validation studies

The proposed FE model of porous FGMEE plate is verified and compared with the studies available in the literature by taking $m = 0$ for perfect functionally graded plate. The normalized natural frequencies for the rectangular simply supported FGMEE plate with an aspect ratio of $b/a = 2$ and a thickness ratio of $h/a = 0.1$, 0.2 are presented in Table 1. Considering the convergence criteria, the results are obtained for various element mesh size. It can be clearly seen from the tabulated results that for a 20 × 20 mesh size, an excellent agreement is achieved with the solutions available in the literature (Milazzo, 2014a). Therefore, for all the subsequent analysis, a mesh size of 20 × 20 is considered.

Table 1
Convergence and validation studies of normalized natural frequencies of FGMEE plate.

h/a		Modes								
		1	2	3	4	5	6	7	8	9
0.2	Present (4 × 4)	6.798	7.923	11.283	13.595	13.642	15.202	18.982	18.693	19.326
	Present (8 × 8)	6.638	7.894	11.213	13.487	13.608	15.183	18.888	18.601	19.295
	Present (12 × 12)	6.623	7.872	11.208	13.462	13.592	15.172	18.854	18.592	19.283
	Present (16 × 16)	6.619	7.863	11.203	13.458	13.588	15.167	18.849	18.583	19.278
	Present (20 × 20)	6.618	7.860	11.198	13.455	13.583	15.161	18.843	18.579	19.273
	Milazzo (Milazzo, 2014a)	6.735	8.223	11.882	13.463	15.049	16.951	19.027	20.178	20.415
0.1	Present (4 × 4)	9.720	13.598	14.909	23.158	27.195	27.290	28.106	31.411	35.006
	Present (8 × 8)	9.663	13.421	14.821	22.986	26.943	27.102	27.994	31.387	34.885
	Present (12 × 12)	9.652	13.417	14.811	22.963	26.932	27.082	27.979	31.372	34.869
	Present (16 × 16)	9.639	13.413	14.807	22.959	26.928	27.078	27.971	31.367	34.862
	Present (20 × 20)	9.637	13.408	14.801	22.952	26.921	27.069	27.967	31.361	34.858
	Milazzo (Milazzo, 2014a)	9.584	12.852	14.733	22.577	25.701	28.339	28.734	32.391	36.341

Table 2
Effect of different porosity distribution on normalized natural frequencies of porous FGMEE plate.

	η	Modes								
		1	2	3	4	5	6	7	8	9
Perfect FG	0.5	4.269	11.075	11.100	22.477	24.014	24.083	41.931	41.983	47.727
	2	4.113	10.697	10.703	21.833	23.235	23.252	40.553	40.566	46.182
Vu	0.5	4.055	10.518	10.544	21.345	22.806	22.874	39.825	39.874	45.329
	2	3.888	10.114	10.119	20.657	21.974	21.987	38.351	38.360	43.678
Vo	0.5	4.216	10.929	10.954	22.107	23.677	23.746	41.310	41.361	46.975
	2	4.057	10.543	10.549	21.452	22.884	22.899	39.913	39.925	45.397
Vx	0.5	4.110	10.670	10.696	21.728	23.155	23.223	40.466	40.516	46.108
	2	3.946	10.274	10.279	21.052	22.341	22.355	39.014	39.024	44.495
Vv	0.5	4.068	10.550	10.577	21.399	22.872	22.944	39.941	39.993	45.460
	2	3.911	10.170	10.177	20.748	22.088	22.106	38.552	38.564	43.897

3.2. Free vibration studies

This section includes the evaluation of free vibration characteristics for FGMEE plates with porosities. Different porosity distributions (*Vu*, *Vo*, *Vx*, and *Vv*) and the porosity volume influencing the natural frequencies are explicitly investigated. The PFGMEE plate considered for the analysis has the following geometrical details: $a/h = 100$; $b/a = 1$; $\eta = 2$. It can be observed from Table 2 that, every porosity distribution has unique influence on the free vibration characteristics of the plate. It is also evident from Table 2 that *Vv* distribution holds the largest influence on the natural frequency of the porous FGMEE plate while *Vu* display the lowest influence. The effect of porosity volume ($0.1 \le m \le 0.5$) on the natural frequencies of porous FGMEE plate is presented in Tables 3–6. It can be clearly seen from these tabulated results that the higher porosity volume reduces the stiffness of the plate and thereby results in lower natural frequencies.

The influence of gradient index (η) on the free vibration characteristics of FGMEE plate is also assessed. Tables 7–9 presents the natural frequencies obtained for perfect FGMEE plate and for the plate with different porosity distributions. It can be seen from these tables that the increase in gradient index decreases the natural frequency. The increase in η transforms the pure $CoFe_2O_4$ composition into combination of $CoFe_2O_4$ and $BaTiO_3$ phases. This combination reduces the stiffness of the porous FGMEE plate. Further, at $\eta = 0$, the plate is completely $CoFe_2O_4$ and possesses the largest natural frequency.

The effect of geometrical parameters such as thickness ratio (a/h) and aspect ratio (b/a) on the free vibration characteristics of the porous FGMEE plate are presented in Tables 10 and 11, respectively. It can be observed from Table 10 that the natural frequencies increases with the increase in thickness ratio for all the porosity distributions considered. Further, it can be noticed from Table 11 that the natural frequency of the porous FGMEE plate decreases for higher aspect ratios. The effect of different boundary conditions on porous FGMEE plate is tabulated in Table 12. It can be clearly noticed from this table that the variation in local flexural rigidity due to change in the constraints at the edges of the plate influence the free vibration characteristics of the porous FGMEE plate. It may also be noticed that among the evaluated boundary conditions, the simply-supported condition (SSSS) shows the lowest natural frequency while the clamped condition (CCCC) attains the highest natural frequency.

3.3. Static studies

In this section, the static characteristics of porous FGMEE plate with different porosity distributions, porosity volume and different gradient index has been analysed by considering a sinusoidal uniformly distributed load across the plate area. The geometrical parameters considered for the study are: $\eta = 2$, $a/h = 100$, $b/a = 1$ and $m = 0.1$. The effect of boundary conditions, thickness ratio, and aspect ratio affecting the primary quantities (displacements and potentials) and the secondary quantities (Stresses, electric displacement and magnetic induction) of the porous FGMEE plate is studied. Fig. 3 (a) – (j) present the effect of different porosity distribution on the various static characteristics of porous FGMEE plate. It can be seen from Fig. 3(a) that the *Vv* porosity distribution has the highest u-displacement while the *Vu* and *Vx* distributions witnessed nearly identical behaviour. The characteristic behaviour of v-displacement in Fig. 3 (b) is similar to that of u-displacement. It is important to notice that the u-displacement clearly display only bending while v-displacement majorly witness stretching. It can also be seen that the stretching is more dominant for *Vu*, *Vo* and *Vx* porosity distributions while the increased contribution of bending along with the stretching is observed for *Vv* distribution. The characteristics of electric potential and magnetic potential for different porosity distribution are displayed in Fig. 3 (c) and (d). It can be seen from Fig. 3 (c) that different porosity distribution has significant influence on the electric potential. Further, it can also be seen that the largest electric potential is witnessed for *Vu* porosity distribution while the lowest is observed for *Vo* distribution. The magnetic potential in Fig. 3(d) display identical characteristics for *Vu*, *Vo* and *Vx* porosity distributions while the *Vv* distribution witnessed the largest magnetic potential. Fig. 3 (e) – (g) display the effect of porosity distribution on various stress quantities and a meagre influence of porosity distribution on stresses is observed. The effect of porosity distribution on magnetic induction is shown in Fig. 3 (i). The *Vu*, *Vo* and *Vx* porosity distributions

Table 3
Effect of porosity factor, m on normalized natural frequencies of porous *Vu* FGMEE plate.

Porosity factor, m	Modes								
	1	2	3	4	5	6	7	8	9
0	4.113	10.697	10.703	21.833	23.235	23.252	40.553	40.566	46.182
0.1	3.888	10.114	10.119	20.657	21.974	21.987	38.351	38.360	43.678
0.2	3.648	9.493	9.496	19.406	20.630	20.638	36.004	36.008	41.012
0.5	2.782	7.255	7.260	14.943	15.795	15.810	27.564	27.581	31.448

Table 4
Effect of porosity factor, m on normalized natural frequencies of porous Vo FGMEE plate.

Porosity factor, m	Modes								
	1	2	3	4	5	6	7	8	9
0	4.113	10.697	10.703	21.833	23.235	23.252	40.553	40.566	46.182
0.1	4.057	10.543	10.549	21.452	22.884	22.899	39.913	39.925	45.397
0.2	4.000	10.387	10.393	21.062	22.526	22.540	39.258	39.269	44.597
0.5	3.822	9.902	9.905	19.835	21.407	21.417	37.186	37.194	42.091

Table 5
Effect of porosity factor, m on normalized natural frequencies of porous Vx FGMEE plate.

Porosity factor, m	Modes								
	1	2	3	4	5	6	7	8	9
0	4.113	10.697	10.703	21.833	23.235	23.252	40.553	40.566	46.182
0.1	3.946	10.274	10.279	21.052	22.341	22.355	39.014	39.024	44.495
0.2	3.772	9.833	9.837	20.237	21.407	21.418	37.404	37.410	42.739
0.5	3.190	8.361	8.361	17.530	18.299	18.300	31.990	31.997	36.934

Table 6
Effect of porosity factor, m on normalized natural frequencies of porous Vv FGMEE plate.

Porosity factor, m	Modes								
	1	2	3	4	5	6	7	8	9
0	4.113	10.697	10.703	21.833	23.235	23.252	40.553	40.566	46.182
0.1	3.911	10.170	10.177	20.748	22.088	22.106	38.552	38.564	43.897
0.2	3.685	9.584	9.592	19.558	20.816	20.836	36.340	36.352	41.383
0.5	2.698	7.048	7.064	14.684	15.389	15.428	26.953	26.972	30.994

Table 7
Effect of gradient index η on normalized natural frequencies of perfect FGMEE plate.

η	Modes								
	1	2	3	4	5	6	7	8	9
0	4.500	11.630	11.690	23.394	25.152	25.310	43.908	44.024	49.999
0.2	4.373	11.325	11.365	22.893	24.526	24.634	42.828	42.908	48.748
0.5	4.269	11.075	11.100	22.477	24.014	24.083	41.931	41.983	47.727
1	4.181	10.862	10.876	22.118	23.576	23.615	41.159	41.188	46.859
2	4.113	10.697	10.703	21.833	23.235	23.252	40.553	40.566	46.182
5	4.044	10.528	10.530	21.544	22.886	22.891	39.936	39.939	45.497

Table 8
Effect of gradient index η on normalized natural frequencies of porous Vu FGMEE plate.

η	Modes								
	1	2	3	4	5	6	7	8	9
0	4.298	11.102	11.163	22.308	24.001	24.164	41.899	42.016	47.719
0.2	4.164	10.782	10.823	21.784	23.347	23.456	40.771	40.851	46.409
0.5	4.055	10.518	10.544	21.345	22.806	22.874	39.825	39.874	45.329
1	3.960	10.291	10.304	20.962	22.339	22.374	38.999	39.025	44.402
2	3.888	10.114	10.119	20.657	21.974	21.987	38.351	38.360	43.678
5	3.816	9.936	9.939	20.355	21.604	21.614	37.700	37.707	42.956

display identical characteristics, and witness no major difference among them. However, the Vv porosity distribution possesses least magnetic induction and display nearly identical magnetic induction at the top and at the bottom of the plate. Furthermore, the effect of porosity distribution on the electric displacement is presented in Fig. 3(j). It can be noticed from the figure that the Vu and Vx distribution show an identical characteristics. It is also noticed that the largest electric displacement is obtained for Vu while the lowest is recorded for Vo.

The comparison of porous and non porous FGMEE plate is studied to emphasize effect of volume of porosity on the static behaviour of the plate. The material distribution of the FGMEE plate is considered for the gradient index $\eta = 2$. The uniform porosity distribution Vu with the porosity index $m = 0.1$ is considered for porous FGMEE plate while for non-porous plate $m = 0$ is considered. Fig. 4 (a) – (j) present the effect

Table 9
Effect of gradient index η on normalized natural frequencies of porous *Vo* FGMEE plate.

η	Modes								
	1	2	3	4	5	6	7	8	9
0	4.450	11.491	11.551	23.033	24.830	24.990	43.300	43.416	49.282
0.2	4.321	11.182	11.223	22.528	24.198	24.305	42.215	42.294	48.014
0.5	4.216	10.929	10.954	22.107	23.677	23.746	41.310	41.361	46.975
1	4.126	10.712	10.726	21.742	23.231	23.269	40.527	40.556	46.088
2	4.057	10.543	10.549	21.452	22.884	22.899	39.913	39.925	45.397
5	3.987	10.373	10.375	21.161	22.530	22.536	39.292	39.296	44.702

Table 10
Effect of thickness ratio (a/h) on normalized natural frequencies of porous FGMEE plate.

	a/h	Modes								
		1	2	3	4	5	6	7	8	9
Perfect FG	10	3.944	9.453	9.459	12.932	12.932	14.552	18.149	18.160	18.295
	20	4.053	10.092	10.098	16.271	20.561	20.577	25.864	25.864	27.704
	100	4.113	10.697	10.703	21.833	23.235	23.252	40.553	40.566	46.182
Vu	10	3.729	8.941	8.945	12.239	12.239	13.765	17.171	17.179	17.314
	20	3.832	9.542	9.546	15.385	19.442	19.453	24.479	24.479	26.204
	100	3.888	10.114	10.119	20.657	21.974	21.987	38.351	38.360	43.678
Vo	10	3.888	9.307	9.312	12.590	12.590	14.311	17.811	17.839	17.850
	20	3.998	9.950	9.956	16.030	20.259	20.273	25.181	25.181	27.258
	100	4.057	10.543	10.549	21.452	22.884	22.899	39.913	39.925	45.397
Vx	10	3.788	9.092	9.097	12.590	12.590	14.014	17.490	17.500	17.811
	20	3.890	9.690	9.695	15.636	19.756	19.769	25.181	25.181	26.667
	100	3.946	10.274	10.279	21.052	22.341	22.355	39.014	39.024	44.495
Vv	10	3.750	8.987	8.993	12.246	12.246	13.832	17.249	17.261	17.326
	20	3.854	9.596	9.603	15.470	19.549	19.566	24.493	24.493	26.334
	100	3.911	10.170	10.177	20.748	22.088	22.106	38.552	38.564	43.897

Table 11
Effect of aspect ratio on normalized natural frequencies of porous FGMEE plate.

	b/a	Modes								
		1	2	3	4	5	6	7	8	9
Perfect FG	0.5	10.238	17.199	31.625	35.213	45.751	66.279	67.908	79.970	92.612
	1	4.113	10.697	10.703	21.833	23.235	23.252	40.553	40.566	46.182
	1.5	2.978	6.283	9.429	13.098	15.780	21.299	26.019	30.635	31.833
	2	2.580	4.747	8.962	9.103	12.810	19.927	20.518	26.889	27.754
	3	2.295	3.467	5.474	8.594	10.341	14.676	19.921	23.921	25.175
Vu	0.5	9.679	16.263	29.911	33.290	43.265	62.745	64.230	75.601	87.566
	1	3.888	10.114	10.119	20.657	21.974	21.987	38.351	38.360	43.678
	1.5	2.815	5.942	8.914	12.391	14.926	20.135	24.604	29.012	30.106
	2	2.439	4.490	8.471	8.610	12.115	18.848	19.394	25.481	26.251
	3	2.169	3.279	5.176	8.123	9.779	13.884	18.828	22.625	23.867
Vo	0.5	10.100	16.950	31.127	34.732	45.063	64.945	66.830	78.864	91.074
	1	4.057	10.543	10.549	21.452	22.884	22.899	39.913	39.925	45.397
	1.5	2.937	6.186	9.296	12.884	15.514	20.990	25.608	29.986	31.321
	2	2.545	4.671	8.837	8.959	12.604	19.598	20.228	26.258	27.300
	3	2.264	3.415	5.394	8.476	10.185	14.423	19.645	23.537	24.550
Vx	0.5	9.823	16.523	30.429	33.793	43.982	64.126	65.352	76.757	89.168
	1	3.946	10.274	10.279	21.052	22.341	22.355	39.014	39.024	44.495
	1.5	2.857	6.043	9.053	12.614	15.201	20.458	25.031	29.683	30.638
	2	2.476	4.56978	8.6023	8.760	12.328	19.190	19.697	26.131	26.723
	3	2.202	3.333	5.260	8.246	9.942	14.147	19.116	23.024	24.510
Vv	0.5	9.735	16.353	30.062	33.483	43.496	62.957	64.550	76.042	88.047
	1	3.911	10.170	10.177	20.748	22.088	22.106	38.552	38.564	43.897
	1.5	2.831	5.972	8.966	12.449	14.998	20.252	24.736	29.092	30.259
	2	2.453	4.512	8.522	8.653	12.177	18.942	19.511	25.522	26.379
	3	2.183	3.297	5.205	8.173	9.832	13.947	18.945	22.738	23.888

of porosity on various parameters. It can be seen from Fig. 4 (a) and (b) that the displacements u and v are higher for the porous plates over non-porous plates. It is evident that the presence of voids/porosities brings down the stiffness of the plate, and there by yields higher deformation. The behaviour of electric potential and magnetic potential is presented in Fig. 4 (c) and (d), respectively. It can be observed from these figures that the electric potential is higher for porous plates over non-porous plates while no major influence of porosity on magnetic potential is observed. The influence of porosity on the normal and the shear stresses as shown in Fig. 4 (e) – (h) and a marginally higher

Table 12
Effect of boundary condition on normalized natural frequencies of porous FGMEE plate.

Porosity distribution	Boundary condition	Modes					
		1	2	3	4	5	6
Perfect FG	SSSS	4.113	10.697	10.703	21.833	23.235	23.252
	FCFC	4.806	5.635	10.066	13.571	14.715	19.764
	CFCF	4.803	5.632	10.067	13.560	14.705	19.774
	SCSC	6.542	14.280	16.155	26.949	28.626	31.065
	CSCS	6.543	14.275	16.163	26.950	28.609	31.086
	CCCC	9.748	19.894	19.900	29.673	32.891	33.023
Vu	SSSS	3.888	10.114	10.119	20.657	21.974	21.987
	FCFC	4.540	5.325	9.519	12.819	13.904	18.688
	CFCF	4.537	5.323	9.520	12.811	13.897	18.696
	SCSC	6.183	13.501	15.267	25.474	27.071	29.354
	CSCS	6.184	13.498	15.273	25.475	27.058	29.370
	CCCC	9.215	18.795	18.800	28.030	31.076	31.203
Vo	SSSS	4.321	11.182	11.223	22.528	24.198	24.305
	FCFC	4.741	5.558	9.912	13.384	14.514	19.462
	CFCF	4.737	5.555	9.913	13.374	14.505	19.471
	SCSC	6.444	14.043	15.913	26.517	28.157	30.630
	CSCS	6.446	14.039	15.921	26.518	28.142	30.650
	CCCC	9.579	19.581	19.587	29.236	32.424	32.552
Vx	SSSS	3.946	10.274	10.279	21.052	22.341	22.355
	FCFC	4.609	5.405	9.679	13.014	14.114	19.003
	CFCF	4.606	5.403	9.680	13.006	14.107	19.011
	SCSC	6.284	13.747	15.519	25.923	27.558	29.808
	CSCS	6.286	13.743	15.525	25.924	27.544	29.826
	CCCC	9.391	19.121	19.126	28.487	31.565	31.696
Vv	SSSS	3.911	10.170	10.177	20.748	22.088	22.106
	FCFC	4.572	5.359	9.570	12.910	13.996	18.791
	CFCF	4.568	5.355	9.571	12.899	13.986	18.801
	SCSC	6.221	13.576	15.364	25.626	27.212	29.548
	CSCS	6.223	13.571	15.373	25.627	27.195	29.571
	CCCC	9.269	18.923	18.930	28.229	31.286	31.412

stresses were seen for porous plate over perfect plates. Fig. 5(i) and (j) present the effect of porosity on magnetic induction and electric displacement, respectively. A significant influence of porosity on electric displacement is seen while the influence of porosity on magnetic induction is negligible.

The effect of aspect ratio on the static behaviour of the FGMEE plate with *Vo* porosity distribution is presented in Fig. 6(a) – (j). From these plots, it can be seen that the higher aspect ratios witness increase in u displacement and decrease in v displacement. Also, the influence on electric potential is found to be more dominant in comparison with magnetic potential. The stress components σ_{xx} and τ_{xy} experiences higher stress magnitude for higher aspect ratio while the influence of aspect ratio on σ_{yy} is marginal. In addition, the transverse shear stress (τ_{xz}) decreases with the increase in aspect ratio. Further, higher aspect ratio results in higher magnetic induction (B_z) and electric displacement (D_z). Fig. 7(a) – (j) display a considerable influence of a/h ratio on the static behaviour of porous FGMEE plate. It is interesting to note that the increase in thickness ratio results in higher primary (u, v, ϕ, and ψ) and secondary quantities (stresses, B_z, and D_z).

The influence of material gradient index on the static behaviour of porous FGMEE plate is represented in Figs. 8–12. The displacements characteristics is observed to be unique for gradient index with every porosity distributions as shown in Fig. 8(a) – (d) and 9(a) – (d). The increase in gradient index decreases the displacements (u and v) for porous FGMEE plate. It is interesting to note that the *Vu*, *Vx*, and *Vv* FGMEE plates display an increase in the displacements with the increase in gradient index while for *Vo* distribution a decrease in displacement is seen. In addition, the electric potential increases with the increase in gradient index as shown in Fig. 10(a) – (d) while Fig. 11(a) – (d) show a decrease in the magnetic potential. Further, the effect of gradient index on the magnetic induction and the electric displacement is presented in Fig. 12(a) – (d) and Fig. 13(a) – (d). It is seen that the magnetic induction decreases with the increase in η while the electric displacement increases with the increase in η. Also, it is noticed that every porosity distribution considered for evaluation presents a different through thickness variation of magnetic induction and electric displacement.

The boundary conditions influencing the static characteristics are presented inFigs. 14–18. It is observed from Fig. 13 (a) – (b) that the displacement u is higher for the mixed boundary condition with clamped free (FCFC) edges. The displacement v presented in Fig. 14 (a) – (b) is higher for the mixed boundary condition CSCS edges and the displacement is found to be minimal for fully clamped plate. The effect of boundary condition on the electric potential and the magnetic potential is shown in Fig. 15(a) and (b) and 16 (a) – (b). It can be seen that the electric and magnetic potential are higher for clamped free (FCFC) plate. It is interesting to note that, among the two porosity distributions considered, *Vo* spared marginally higher electric potential over *Vu*. The influence of porosity distribution on magnetic potential is negligible. In addition, the magnetic induction and the electric displacement is higher for simply supported plate and they are observed to be minimal for clamped plate as observed in Fig. 18(a) and (b) and 19 (a) – (b).

4. Conclusions

Current article includes the evaluation of free vibration and static behaviour of porous FGMEE plate. The porosity is considered to be local density and approximated via modified power law. Four different porosity distributions are considered for the first time. The constitutive equations accounting the coupled fields and the principle of virtual work is utilised to form the FE model. The free vibration studies reveal that the porosity in the material significantly affects the natural frequencies of the FGMEE plate. Although, every porosity distribution produces unique free vibration behaviour, *Vv* possesses the largest influence on the natural frequency while *Vu* witnesses the least influence. Higher porosity volume reduces the natural frequency of the plate. The increase in gradient index decreases the natural frequency of porous FGMEE plate irrespective of distribution type. Higher thickness ratio increases the natural frequency while higher aspect ratio decreases the natural frequency. In addition, the static studies reveal certain interesting outcomes. Displacements are largely influenced by the porosity and the highest displacement is associated with *Vv* distribution. *Vu* distribution attains the largest electric potential and electric displacement while *Vv* distribution projects the largest magnetic potential and magnetic induction. Further, the displacements and the electric potential are higher for porous plate over non-porous plate while no major influence is seen on magnetic potential. Stresses are marginally higher for porous plates over perfect plates. Although, porosity significantly influences the electric displacement, no major influence of porosity on magnetic induction is observed. Geometrical parameters such as aspect ratio and thickness ratio display a major influence on static structural characteristics of porous FGMEE plate. The gradient index and the boundary conditions produce interesting response characteristics for PFGMEE plate.

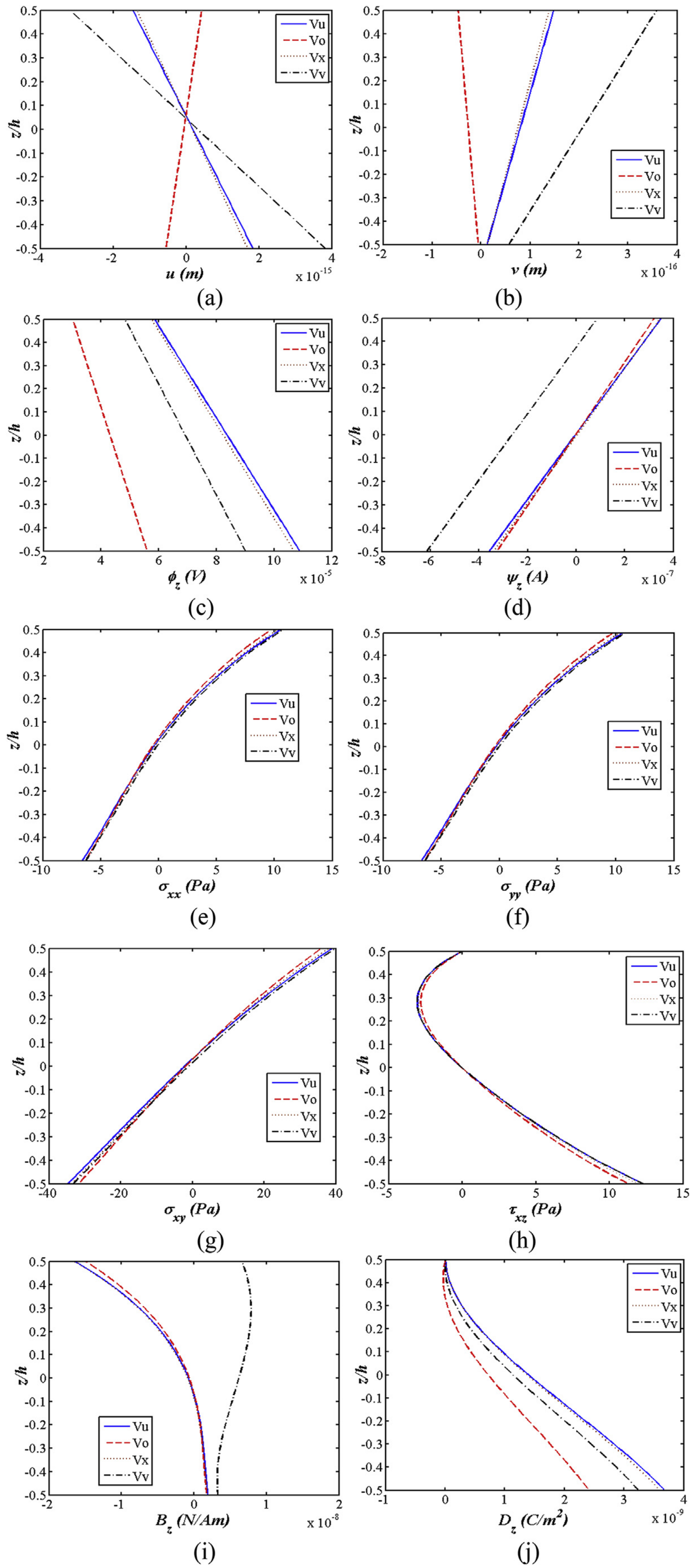

Fig. 3. Effect of different porosity distribution on (a) u (b) v (c) ϕ_z (d) ψ_z (e) σ_{xx} (f) σ_{yy} (g) σ_{xy} (h) τ_{xz} (i) B_z (j) D_z.

B_z (j) D_z

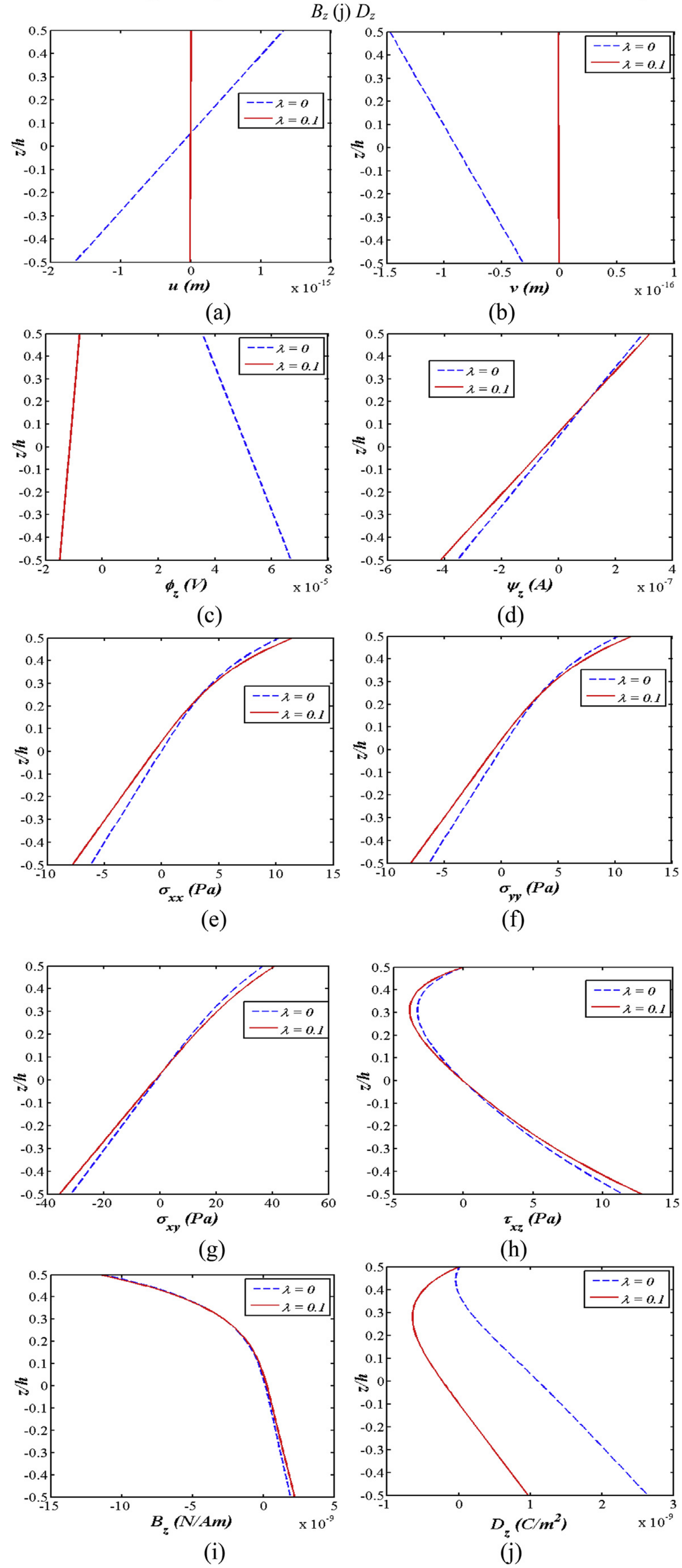

Fig. 4. Effect of porosity on (a) u (b) v (c) ϕ_z (d) ψ_z (e) σ_{xx} (f) σ_{yy} (g) σ_{xy} (h) τ_{xz} (i) B_z (j) D_z @ η = 5.

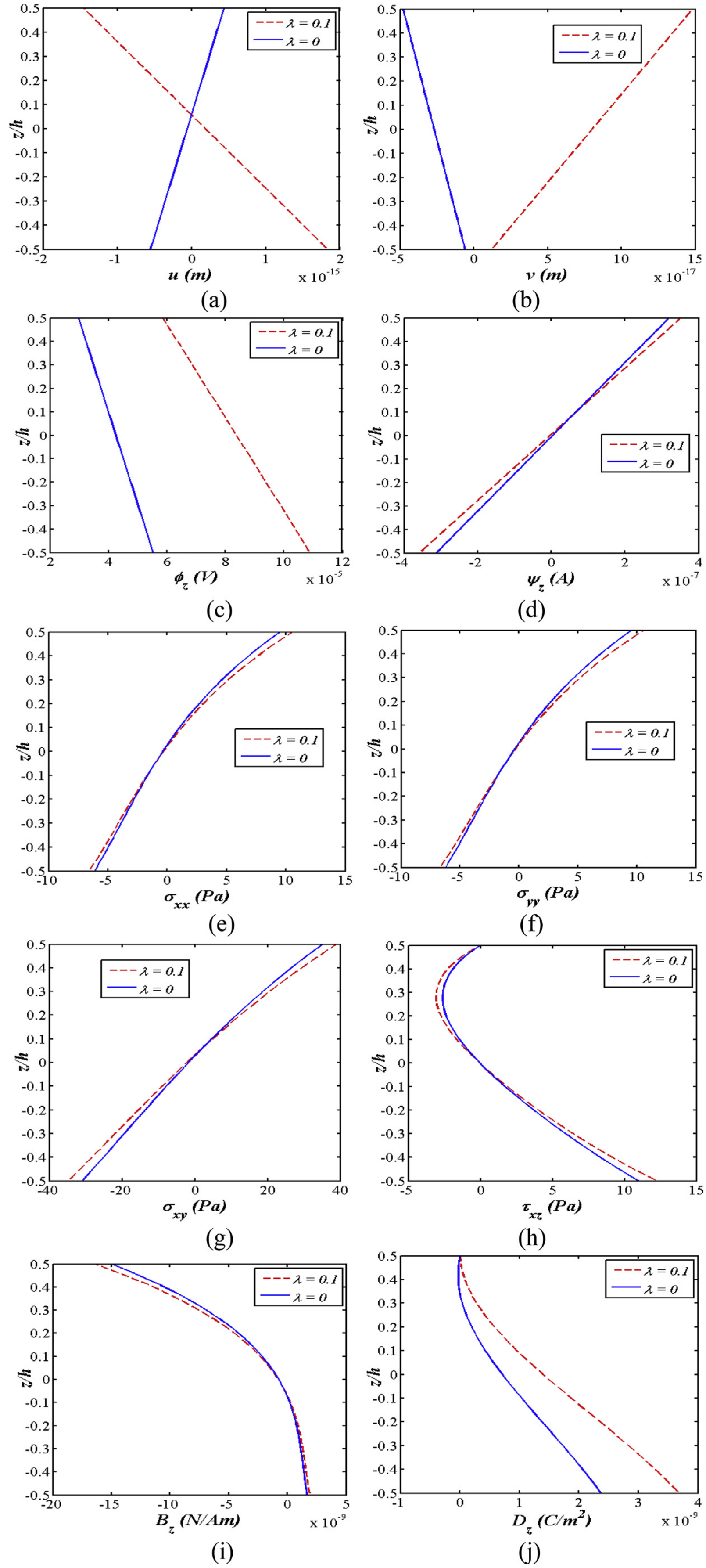

Fig. 5. Effect of porosity on (a) u (b) v (c) ϕ_z (d) ψ_z (e) σ_{xx} (f) σ_{yy} (g) σ_{xy} (h) τ_{xz} (i) B_z (j) D_z @ $\eta = 2$.

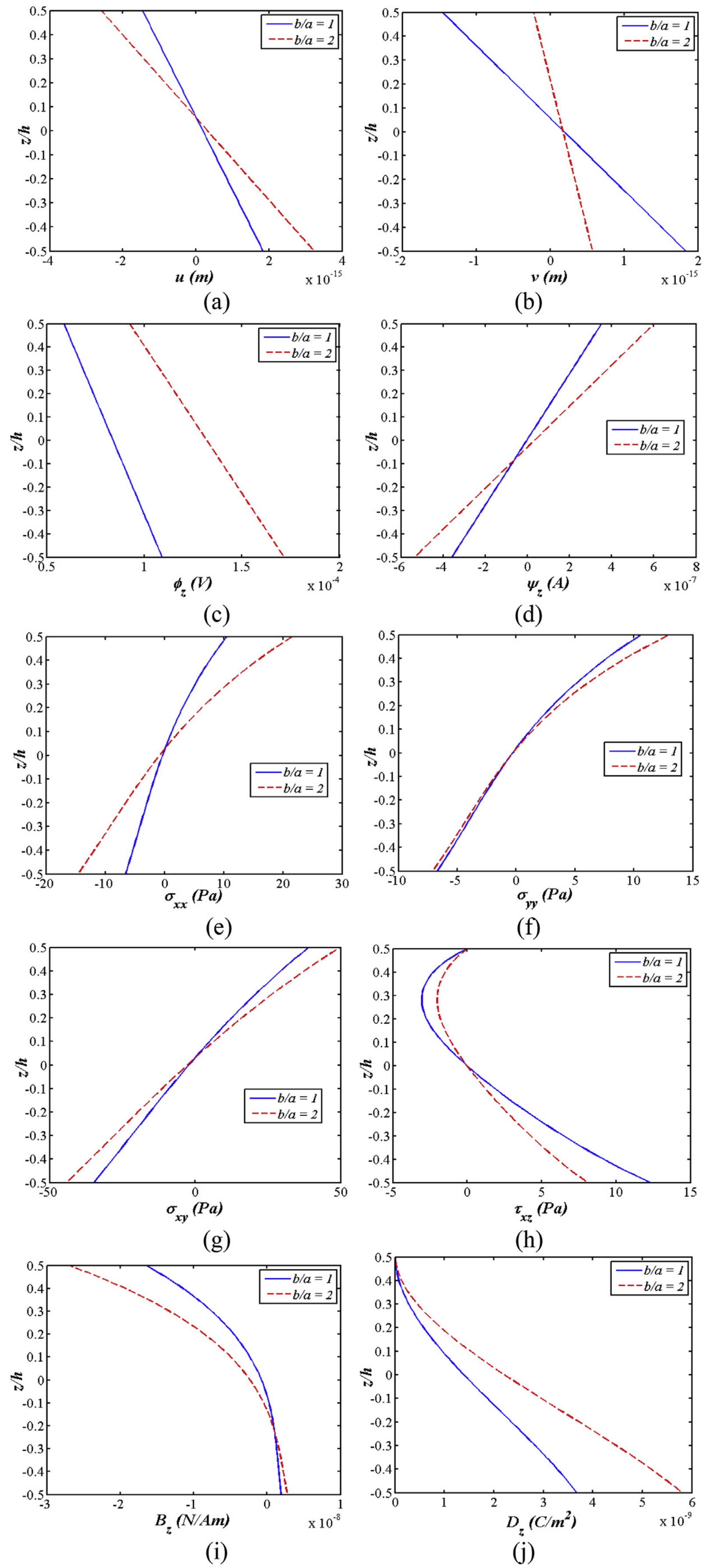

Fig. 6. Effect of aspect ratio (b/a) on (a) u (b) v (c) ϕ_z (d) ψ_z (e) σ_{xx} (f) σ_{yy} (g) σ_{xy} (h) τ_{xz} (i) B_z (j) D_z for Vo (m = 0.1 a = b = 100h, η = 2).

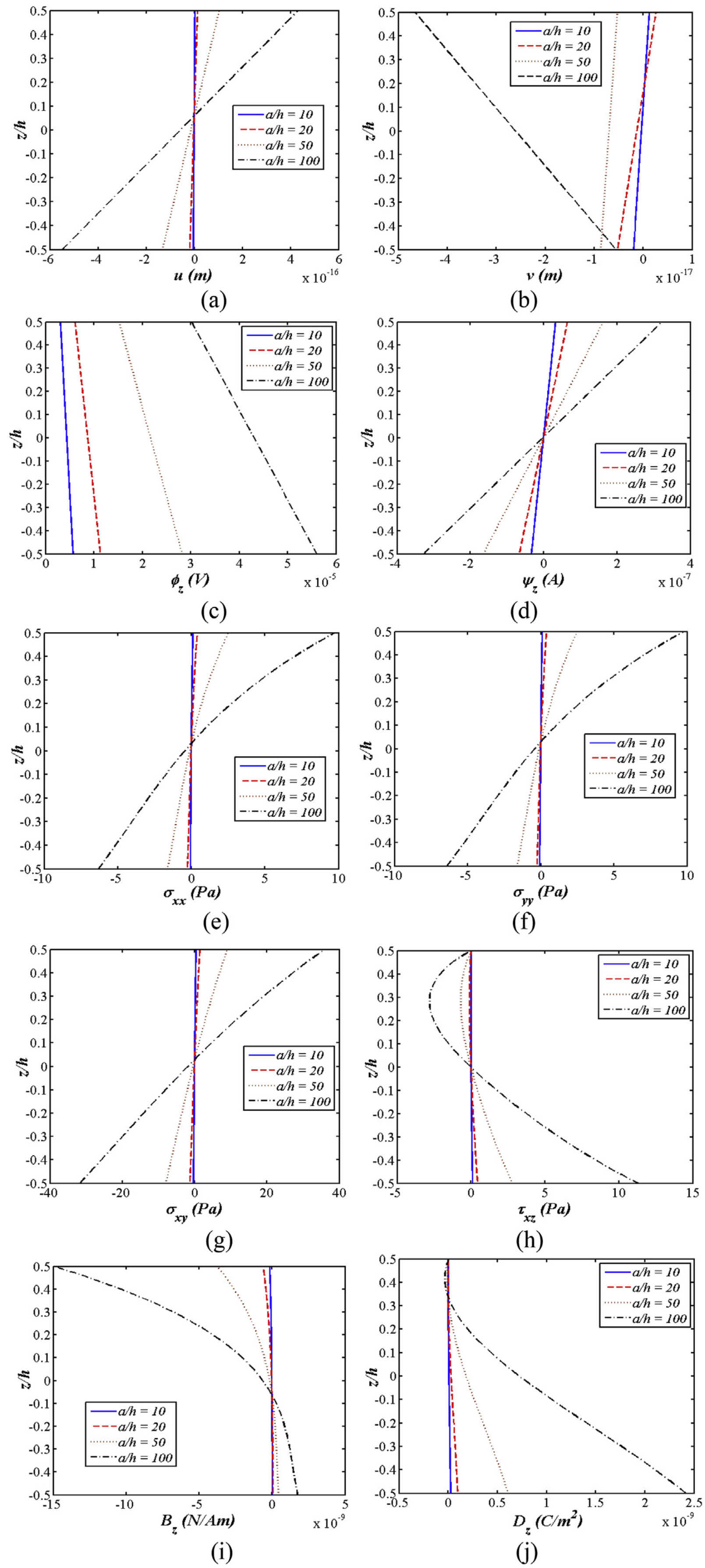

Fig. 7. Effect of thickness ratio (a/h) on (a) u (b) v (c) ϕ_z (d) ψ_z (e) σ_{xx} (f) σ_{yy} (g) σ_{xy} (h) τ_{xz} (i) B_z (j) D_z for Vo (m = 0.1 a = b = 100h, η = 2).

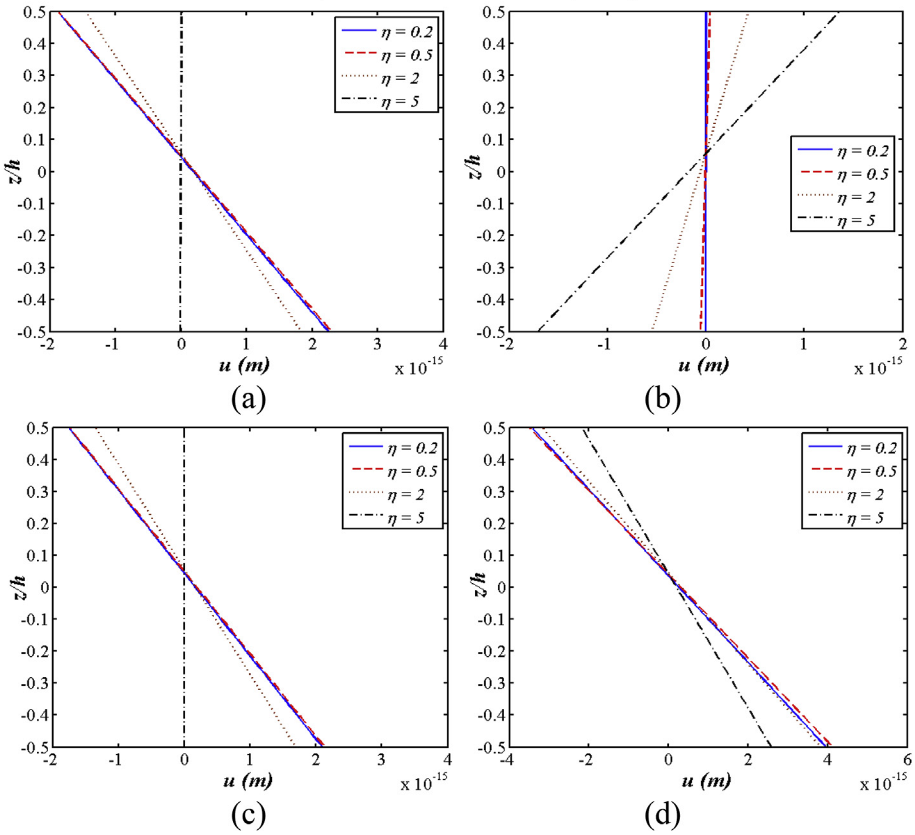

Fig. 8. Effect of gradient index on u (a) *Vu* (b) *Vo* (c) *Vx* (d) *Vv*.

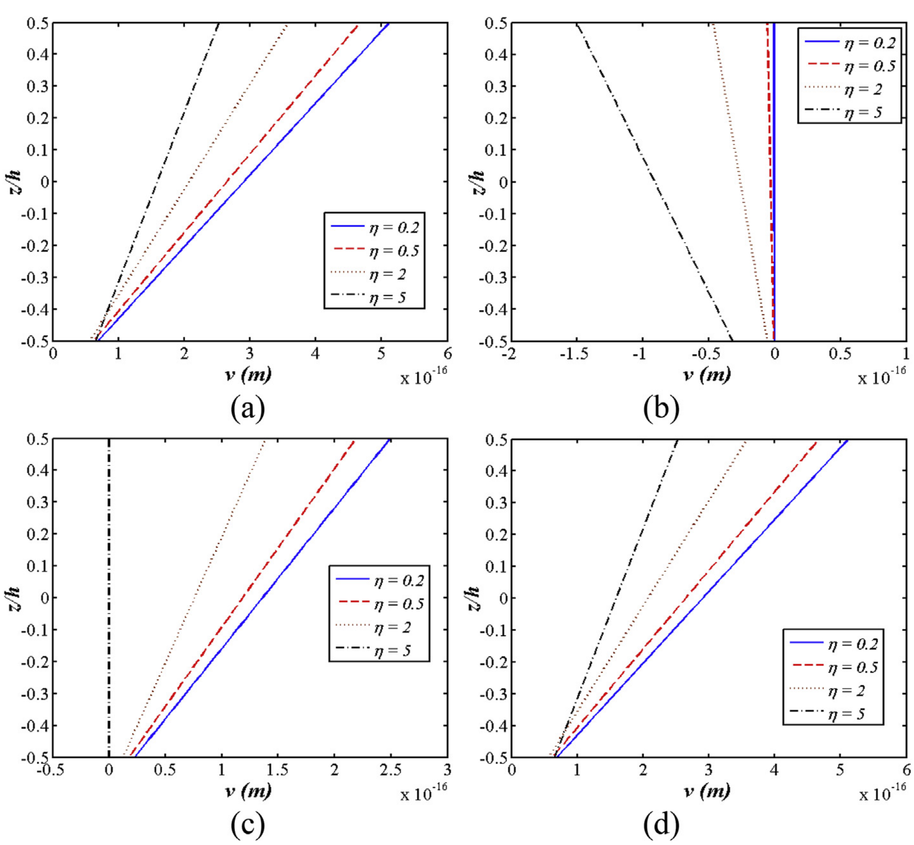

Fig. 9. Effect of gradient index on v (a) *Vu* (b) *Vo* (c) *Vx* (d) *Vv*.

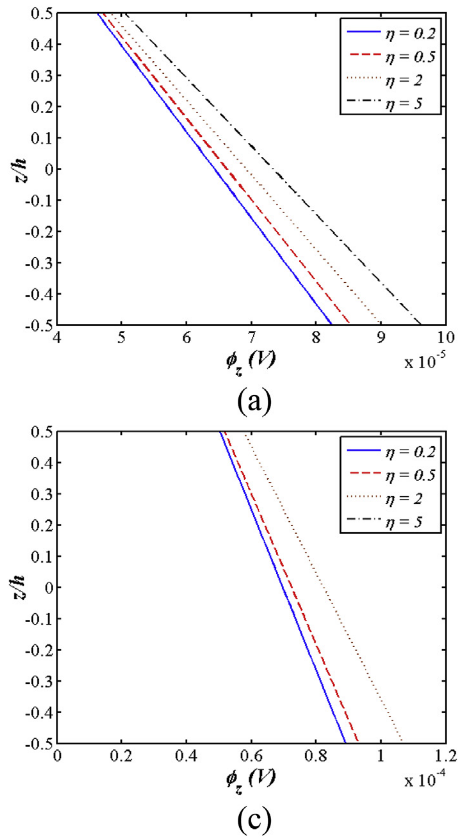

Fig. 10. Effect of gradient index on electric potential (a) *Vu* (b) *Vo* (c) *Vx* (d) *Vv*.

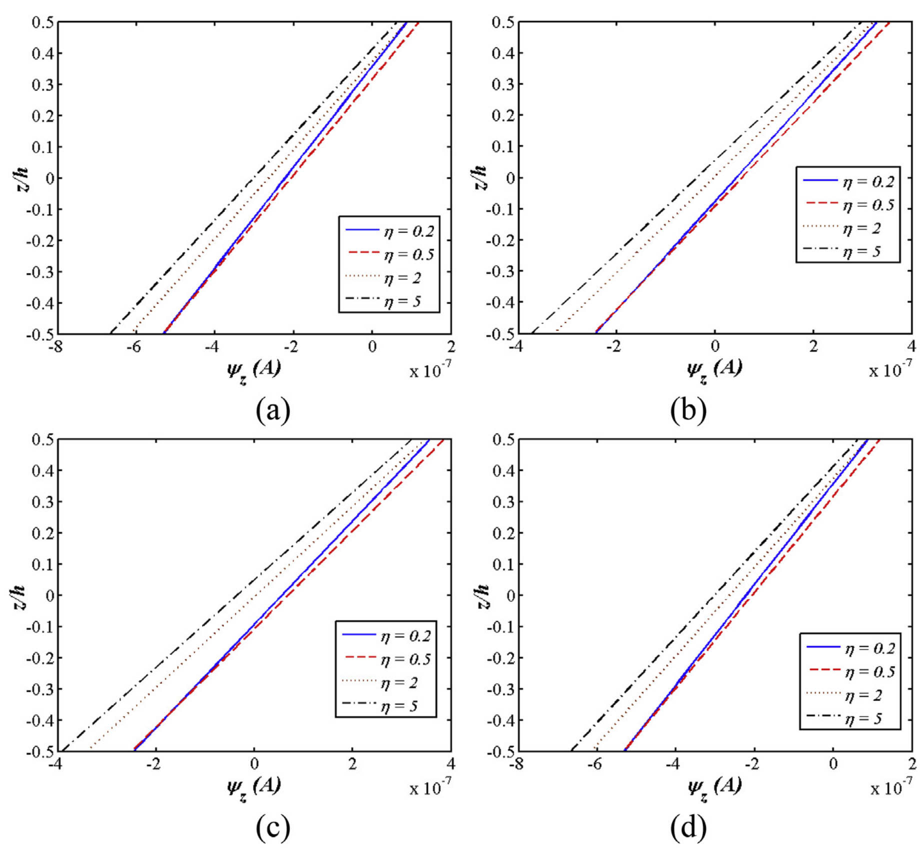

Fig. 11. Effect of gradient index on magnetic potential (a) *Vu* (b) *Vo* (c) *Vx* (d) *Vv*.

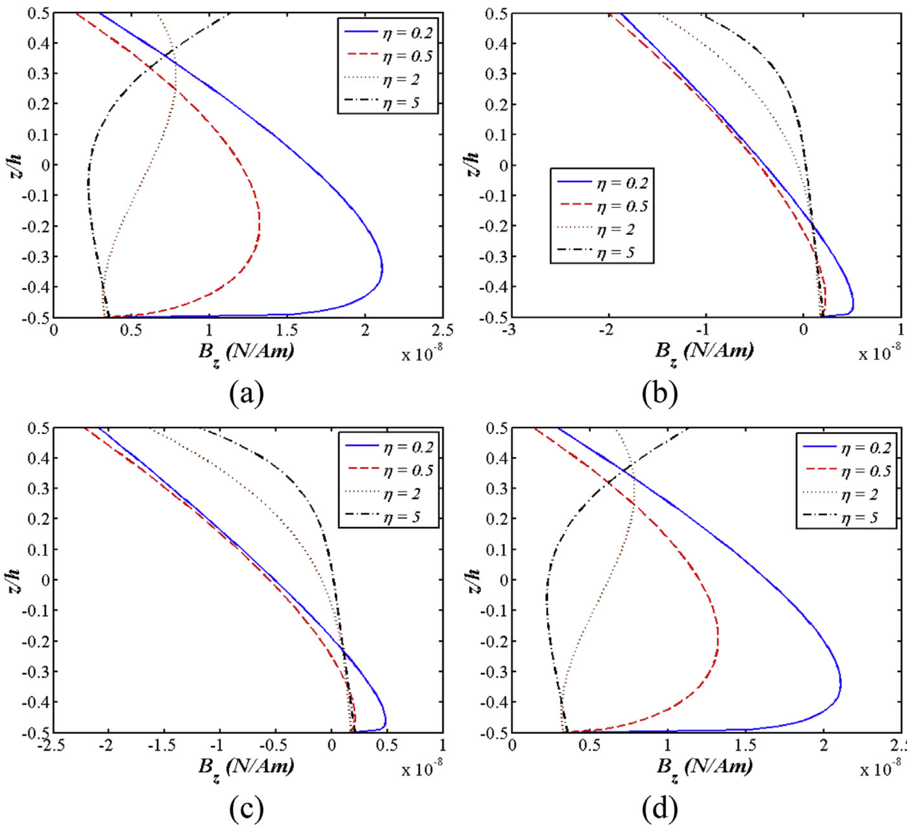

Fig. 12. Effect of gradient index on magnetic induction (a) *Vu* (b) *Vo* (c) *Vx* (d) *Vv*.

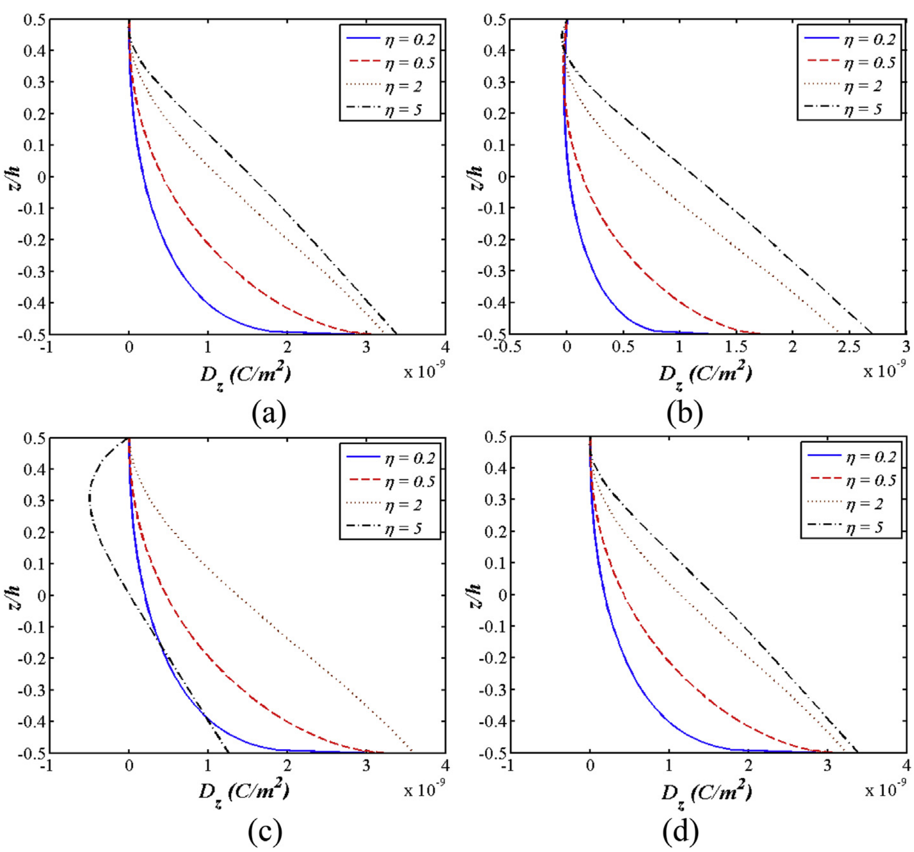

Fig. 13. Effect of gradient index on electric displacement (a) *Vu* (b) *Vo* (c) *Vx* (d) *Vv*.

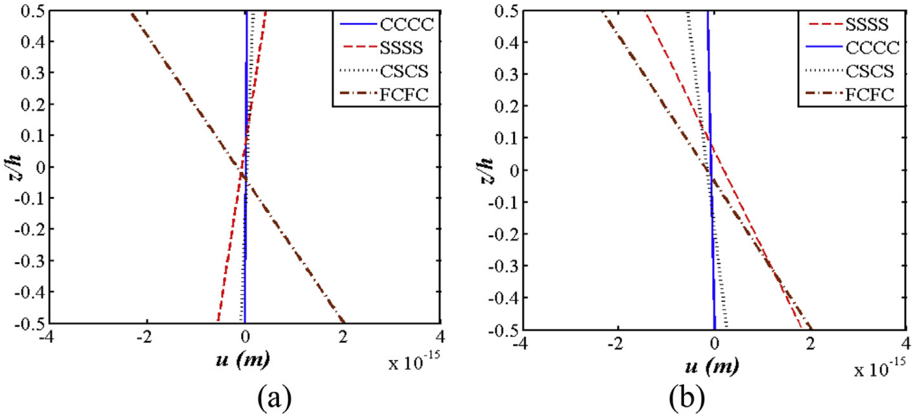

Fig. 14. Effect of boundary condition on u (a) *Vu* (b) *Vo*.

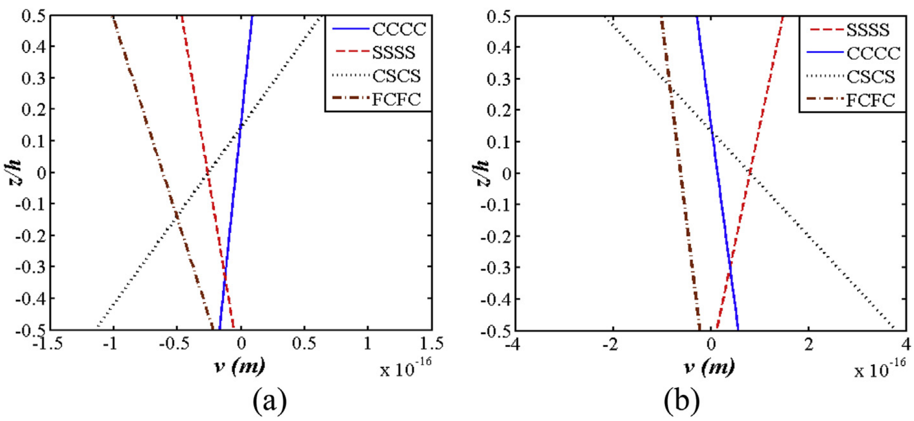

Fig. 15. Effect of boundary condition on v (a) *Vu* (b) *Vo*.

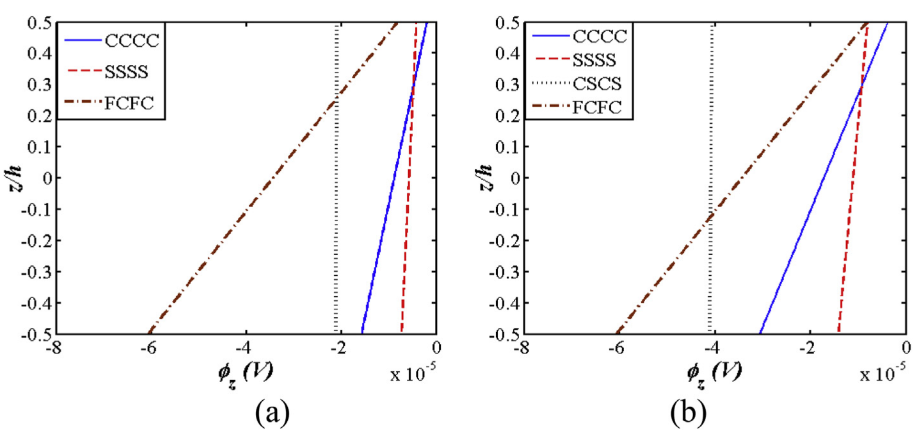

Fig. 16. Effect of boundary condition on electric potential (a) *Vu* (b) *Vo*.

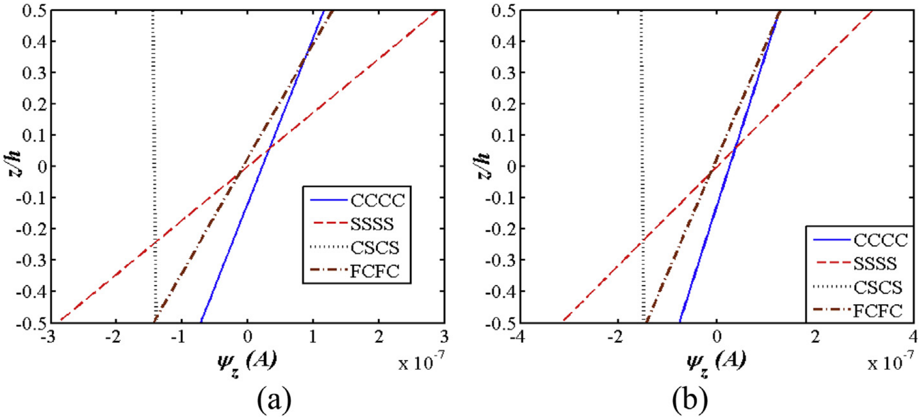

Fig. 17. Effect of boundary condition on magnetic potential (a) *Vu* (b) *Vo*.

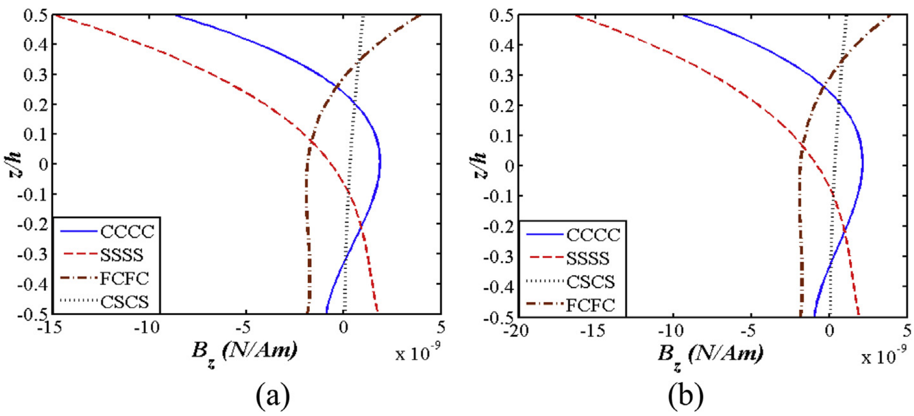

Fig. 18. Effect of boundary condition on magnetic induction (a) *Vu* (b) *Vo*.

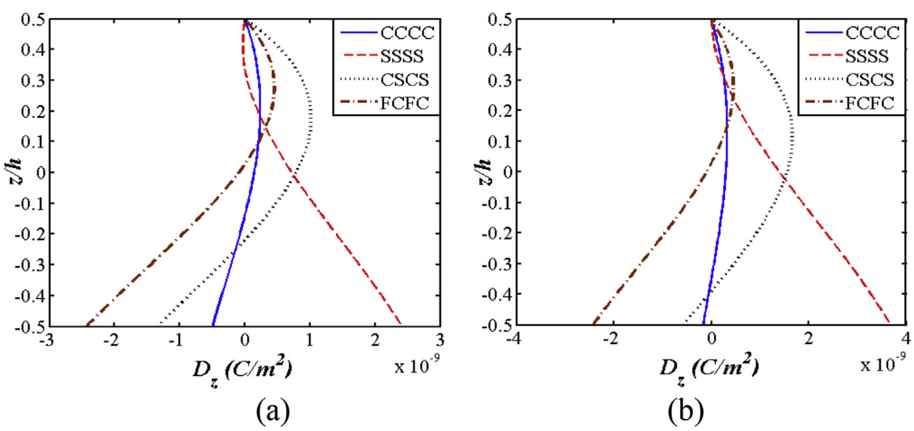

Fig. 19. Effect of boundary condition on electric displacement (a) *Vu* (b) *Vo*.

Appendix

The matrices and the vectors appearing in Eqs. 19–22 are given as follows:

$[\mathrm{k}_{\mathrm{tt}}^{\mathrm{el}}] = [\mathrm{k}_{\mathrm{tb}}^{\mathrm{el}}] + [\mathrm{k}_{\mathrm{ts}}^{\mathrm{el}}][\mathrm{k}_{\mathrm{tr}}^{\mathrm{el}}] = [\mathrm{k}_{\mathrm{trb}}^{\mathrm{el}}] + [\mathrm{k}_{\mathrm{trs}}^{\mathrm{el}}][\mathrm{k}_{\mathrm{rr}}^{\mathrm{el}}] = [\mathrm{k}_{\mathrm{rrb}}^{\mathrm{el}}] + [\mathrm{k}_{\mathrm{rrs}}^{\mathrm{el}}]$

$[\mathrm{k}_{\mathrm{t}\phi}^{\mathrm{el}}] = [\mathrm{k}_{\phi\mathrm{t}}^{\mathrm{el}}]^{T}[\mathrm{k}_{\mathrm{t}\psi}^{\mathrm{el}}] = [\mathrm{k}_{\psi\mathrm{t}}^{\mathrm{el}}]^{T}[\mathrm{k}_{\mathrm{r}\phi}^{\mathrm{el}}] = [\mathrm{k}_{\phi r}^{\mathrm{el}}]^{T}[\mathrm{k}_{\mathrm{r}\psi}^{\mathrm{el}}] = [\mathrm{k}_{\psi r}^{\mathrm{el}}]^{T}$

where,

$$[\mathrm{k}_{\mathrm{tb}}^{\mathrm{el}}] = \int_0^{a_{el}}\int_0^{b_{el}} [\mathrm{b}_{\mathrm{tb}}]^T[D_{tb}][\mathrm{b}_{\mathrm{tb}}]dx\, dy\, [\mathrm{k}_{\mathrm{ts}}^{\mathrm{el}}] = \int_0^{a_{el}}\int_0^{b_{el}} [\mathrm{b}_{\mathrm{ts}}]^T[D_{ts}][\mathrm{b}_{\mathrm{ts}}]dx\, dy\, [\mathrm{k}_{trb}^{\mathrm{el}}] = \int_0^{a_{el}}\int_0^{b_{el}} [\mathrm{b}_{\mathrm{tb}}]^T[D_{trb}][\mathrm{b}_{\mathrm{rb}}]dx\, dy$$

$$[\mathrm{k}_{rrb}^{\mathrm{el}}] = \int_0^{a_{el}}\int_0^{b_{el}} [\mathrm{b}_{\mathrm{rb}}]^T [D_{rrb}] [\mathrm{b}_{\mathrm{rb}}] dx\, dy [\mathrm{k}_{rrs}^{\mathrm{el}}] = \int_0^{a_{el}}\int_0^{b_{el}} [\mathrm{b}_{\mathrm{rs}}]^T [D_{rrs}] [\mathrm{b}_{\mathrm{rs}}] dx\, dy$$

$$[\mathrm{k}_{\mathrm{t}\psi}^{\mathrm{el}}] = \int_0^{a_{el}}\int_0^{b_{el}} [\mathrm{b}_{\mathrm{tb}}]^T [D_{t\psi}] [N_\psi]\, dx\, dy [\mathrm{k}_{r\psi}^{\mathrm{el}}] = \int_0^{a_{el}}\int_0^{b_{el}} [\mathrm{b}_{\mathrm{rb}}]^T [D_{r\psi}] [N_\psi]\, dx\, dy$$

$$[\mathrm{k}_{\phi\phi}^{\mathrm{el}}] = \int_0^{a_{el}}\int_0^{b_{el}} [N_\phi]^T [D_{\phi\phi}] [N_\phi]\, dx\, dy [\mathrm{k}_{\psi\psi}^{\mathrm{el}}] = \int_0^{a_{el}}\int_0^{b_{el}} [N_\psi]^T [D_{\psi\psi}] [N_\psi]\, dx\, dy$$

where, a^{el} and b^{el} corresponds to the length and width of the element under consideration. $[D_{tb}]$, $[D_{ts}]$, $[D_{trb}]$, $[D_{trs}]$, $[D_{rrb}]$, $[D_{rrs}]$, $[D_{t\phi}]$, $[D_{r\phi}]$, $[D_{t\psi}]$, $[D_{r\psi}]$, $[D_{\phi\phi}]$ and $[D_{\psi\psi}]$ are the rigidity matrices appearing in Eq. (23) are given as follows:

$$[D_{tb}] = \int_{-h/2}^{h/2} [C_b]\, dz [D_{ts}] = \int_{-h/2}^{h/2} [C_s]\, dz,$$

$$[D_{trb}] = \int_{-h/2}^{h/2} [C_b]\, [Z_1]\, dz [D_{trs}] = \int_{-h/2}^{h/2} [C_s]\, [Z_2]\, dz$$

$$[D_{rrb}] = \int_{-h/2}^{h/2} [Z_1]^T [C_b]\, [Z_1]\, dz [D_{rrs}] = \int_{-h/2}^{h/2} [Z_2]^T [C_s]\, [Z_2]\, dz$$

$$[D_{t\phi}] = \int_{-h/2}^{h/2} \{e_b(z)\}\frac{1}{h}dz \quad [D_{t\psi}] = \int_{-h/2}^{h/2} \{q_b(z)\}\frac{1}{h}\, dz$$

$$[D_{r\phi}] = \int_{-h/2}^{h/2} [z_1]^T\{e_b(z)\}\frac{1}{h}\, dz \quad [D_{r\psi}] = \int_{-h/2}^{h/2} [z_1]^T\{q_b(z)\}\frac{1}{h}\, dz$$

$$[D_{\phi\phi}] = \frac{\xi_{33}(z)}{h}\begin{bmatrix} 1 & 0 \\ 0 & 1 \end{bmatrix}[D_{\psi\psi}] = \frac{1}{h}\mu_{33}(z)$$

References

Barati, M.R., 2018. A general nonlocal stress-strain gradient theory for forced vibration analysis of heterogeneous porous nanoplates. Eur. J. Mech. Solid. 67, 215–230.

Barati, M.R., Shahverdi, H., 2017. Aero-hygro-thermal stability analysis of higher-order refined supersonic FGM panels with even and uneven porosity distributions. J. Fluids Struct 73, 125–136.

Barati, M.R., Shahverdi, H., Zenkour, A.M., 2017. Electro-mechanical vibration of smart piezoelectric FG plates with porosities according to a refined four-variable theory. Mech. Adv. Mater. Struct. 24 (12), 987–998.

Boomgaard, V.J., Born, R.A., 1978. Sintered magnetoelectric composite material BaTiO3-Ni (Co, Mn)Fe2O4. J. Mater. Sci. 13 (7), 1538–1548.

Buchanan, G.R., 2004. Layered versus multiphase magneto-electro-elastic composites. Compos. Part B (Engg) 35 (5), 413–420.

Chen, J.Y., Heyliger, P.R., Pan, E., 2014. Free vibration of three-dimensional multilayered magneto-electro-elastic plates under clamped/free boundary conditions. J. Sound Vib. 333, 4017–4029.

Ebrahimi, F., Rastgoo, A., 2009. Nonlinear vibration of smart circular functionally graded plates coupled with piezoelectric layers. Int. J. Mech. Mater. Des. 5 (2), 157–165.

Ebrahimi, F., Rastgoo, A., 2011. Nonlinear vibration analysis of piezo-thermo-electrically actuated functionally graded circular plates. Arch. Appl. Mech. 81 (3), 361–383.

Ebrahimi, F., Naei, M.H., Rastgoo, A., 2009. Geometrically nonlinear vibration analysis of piezoelectrically actuated FGM plate with an initial large deformation. J. Mech. Sci. Technol. 23 (8), 2107–2124.

Ebrahimi, F., Jafari, A., Barati, M.R., 2017a. Vibration analysis of magneto-electro-elastic heterogeneous porous material plates resting on elastic foundations. Thin-Wall. Struct 119, 33–46.

Ebrahimi, F., Jafari, A., Barati, M.R., 2017b. Free vibration analysis of smart porous plates subjected to various physical fields considering neutral surface position. Arab. J. Sci. Eng 42 (5), 1865–1881.

Hildebrand, F.B., Reissner, E., Thomas, G.B., 1949. Notes on the foundations of the theory of small displacements of orthotropic shells. NACA Technical Note 1833.

Kattimani, S.C., Ray, M.C., 2014a. Smart damping of geometrically nonlinear vibrations of magneto-electro-elastic plates. Compos. Struct. 114, 51–63.

Kattimani, S.C., Ray, M.C., 2014b. Active control of large amplitude vibrations of smart magneto-electro-elastic doubly curved shells. Int. J. Mech. Mater. Des. 10, 351–378.

Kattimani, S.C., Ray, M.C., 2015. Control of geometrically nonlinear vibrations of functionally graded Magneto-electro-elastic plates. Int. J. Mech. Sci. 99, 154–167.

Khor, K.A., Gu, Y.W., 2000. Effects of residual stress on the performance of plasma sprayed functionally graded ZrO_2/NiCoCrAlY coatings. Mater. Sci. Eng. A 277 (1), 64–76.

Kiran, M.C., Kattimani, S.C., 2017. Buckling characteristics and static studies of multilayered magneto-electro-elastic plate. Struct. Eng. Mech. 64 (6), 751–763.

Kiran, M.C., Kattimani, S.C., 2018a. Buckling of skew magneto-electro-elastic plates under inplane loading. J. Intell. Material Syst. Struct 1–17. http://dx.doi.org/10.1177/1045389X18758191.

Kiran, M.C., Kattimani, S.C., 2018b. Free vibration and static analysis of functionally graded skew magneto-electro-elastic plate. Smart Mater. Struct. 21 (6). https://doi.org/10.12989/sss.2018.21.4.000.

Kiran, M.C., Kattimani, S.C., 2018c. Porosity influence on structural behaviour of skew functionally graded magneto-electro-elastic plate. Compos. Struct. 191 (6), 36–77.

Lage, R.G., Soares, C.M.M., Soares, C.A.M., Reddy, J.N., 2004. Layerwise partial mixed finite element analysis of magneto-electro-elastic plates. Comput. Struct. 82, 1293–1301.

Liu, J., Zhang, P., Lin, G., Wang, W., Lu, S., 2016. Solutions for the magneto-electro-elastic plate using the scaled boundary finite element method. Eng. Anal. Bound. Elem. 68, 103–114.

Milazzo, A., 2014a. Refined equivalent single layer formulations and finite elements for smart laminates free vibrations. Compos. Part-B (Engg) 61, 238–253.

Milazzo, A., 2014b. Large deflection of magneto-electro-elastic laminated plates. Appl. Math. Model. 38 (5), 1737–1752.

Milazzo, A., 2016. Unified formulation for a family of advanced finite elements for smart multilayered plates. Mech. Adv. Mater. Struc 23 (9), 971–980.

Miyamoto, Y., Kaysser, W., Rabin, B., Kawasaki, A., Ford, R.G., 2013. Functionally Graded Materials: Design, Processing and Applications. Springer Sci. Busi. Media, pp. 5.

Mortensen, A., Suresh, S., 1995. Functionally graded metals and metal-ceramic composites. Part 1 Processing. Int. Mater. Rev. 40 (6), 239–265.

Pan, E., 2001. Exact solution for simply supported and multilayered magneto-electro-elastic plates. J. Appl. Mech.-T 68, 608–618.

Pan, E., Han, F., 2005. Exact solutions for functionally graded and layered magneto-electro-elastic plates. Int. J. Eng. Sci. 43, 321–339.

Pan, E., Heyliger, P.R., 2003. Exact solutions for magneto-electro-elastic laminates in cylindrical bending. Int. J. Solids Struct 40 (24), 6859–6876.

Peng, X., Yan, M., Shi, W., 2007. A new approach for the preparation of functionally graded materials via slip casting in a gradient magnetic field. Scr. Mater 56 (10), 907–909.

Pompe, W., Worch, H., Epple, Friess M., Gelinsky, M., Greil, P., Hempel, U., Scharnweber, D., Schulte, K., 2003. Functionally graded materials for biomedical applications. Mater. Sci. Eng.: A 362 (1), 40–60.

Ramirez, F., Heyliger, P.R., Pan, E., 2006. Free vibration response of two-dimensional magneto-electro-elastic plates. J. Sound Vib. 292, 626–644.

Simoes Moita, J.M., Mota Soares, C.M., Mota Soares, C.A., 2009. Analyses of Magneto-electro-elastic plates using a higher order finite element model. Compos. Struct. 91,

421–426.
Song, C., Xu, Z., Li, J., 2007. Structure of in situ Al/Si functionally graded materials by electromagnetic separation method. Mater. Des. 28 (3), 1012–1015.
Vinyas, M., Kattimani, S.C., 2017. Static studies of stepped functionally graded magneto-electro-elastic beam subjected to different thermal loads. Compos. Struct. 163, 216–237.
Waksmanski, N., Pan, E., 2016. An analytical three-dimensional solution for free vibration of a magneto-electro-elastic plate considering the nonlocal effect. J Intel. Mater. Sys. Struct 28, 1501–1513.
Wang, Y.Q., Wan, Y.H., Zhang, Y.F., 2017. Vibrations of longitudinally travelling functionally graded material plates with porosities. Eur. J. Mech. Solid. 2017 (66), 55–68.
Watanabe, Y., Eryu, H., Matsuura, K., 2001. Evaluation of three-dimensional orientation of Al 3 Ti platelet in Al-based functionally graded materials fabricated by a centrifugal casting technique. Acta Mater. 49 (5), 775–783.
Wattanasakulpong, N., Prusty, B.G., Kelly, D.W., Hoffman, M., 2012. Free vibration analysis of layered functionally graded beams with experimental validation. Mater. Des. 36, 182–190.
Zhu, J., Lai, Z., Yin, Z., Jeon, J., Lee, S., 2001. Fabrication of ZrO 2–NiCr functionally graded material by powder metallurgy. Mater. Chem. Phy. 68 (1), 130–135.